The Astrophysical Journal, 742:116 (19pp), 2011 December 1 doi:10.1088/0004-637X/742/2/116

HAT-P-20b–HAT-P-23b: FOUR MASSIVE TRANSITING EXTRASOLAR PLANETS*

G. Á. Bakos[1,12], J. Hartman[1], G. Torres[1], D. W. Latham[1], Géza Kovács[2], R. W. Noyes[1], D. A. Fischer[3,4], J. A. Johnson[5], G. W. Marcy[6], A. W. Howard[6], D. Kipping[1,7], G. A. Esquerdo[1], A. Shporer[8,9], B. Béky[1], L. A. Buchhave[10], G. Perumpilly[1], M. Everett[1], D. D. Sasselov[1], R. P. Stefanik[1], J. Lázár[11], I. Papp[11], and P. Sári[11]
[1] Harvard-Smithsonian Center for Astrophysics, Cambridge, MA, USA; gbakos@cfa.harvard.edu
[2] Konkoly Observatory, Budapest, Hungary
[3] Astronomy Department, Yale University, New Haven, CT, USA
[4] Department of Physics and Astronomy, San Francisco State University, San Francisco, CA, USA
[5] California Institute of Technology, Department of Astrophysics, MC 249-17, Pasadena, CA, USA
[6] Department of Astronomy, University of California, Berkeley, CA, USA
[7] Department of Physics, University College London, Gower St., London WC1E 6BT, UK
[8] LCOGT, 6740 Cortona Drive, Santa Barbara, CA, USA
[9] Department of Physics, Broida Hall, UC Santa Barbara, CA, USA
[10] Niels Bohr Institute, Copenhagen University, DK-2100 Copenhagen, Denmark
[11] Hungarian Astronomical Association, Budapest, Hungary
Received 2010 August 1; accepted 2011 August 15; published 2011 November 15

ABSTRACT

We report the discovery of four relatively massive (2–7 M_J) transiting extrasolar planets. HAT-P-20b orbits the moderately bright $V = 11.339$ K3 dwarf star GSC 1910-00239 on a circular orbit, with a period $P = 2.875317 \pm 0.000004$ days, transit epoch $T_c = 2455080.92661 \pm 0.00021$ ($\mathrm{BJD_{UTC}}$), and transit duration 0.0770 ± 0.0008 days. The host star has a mass of $0.76 \pm 0.03\, M_\odot$, radius of $0.69 \pm 0.02\, R_\odot$, effective temperature 4595 ± 80 K, and metallicity $[\mathrm{Fe/H}] = +0.35 \pm 0.08$. The planetary companion has a mass of $7.246 \pm 0.187\, M_J$ and a radius of $0.867 \pm 0.033\, R_J$ yielding a mean density of 13.78 ± 1.50 g cm^{-3}. HAT-P-21b orbits the $V = 11.685$ G3 dwarf star GSC 3013-01229 on an eccentric ($e = 0.228 \pm 0.016$) orbit, with a period $P = 4.124481 \pm 0.000007$ days, transit epoch $T_c = 2454996.41312 \pm 0.00069$, and transit duration 0.1530 ± 0.0027 days. The host star has a mass of $0.95 \pm 0.04\, M_\odot$, radius of $1.10 \pm 0.08\, R_\odot$, effective temperature 5588 ± 80 K, and metallicity $[\mathrm{Fe/H}] = +0.01 \pm 0.08$. The planetary companion has a mass of $4.063 \pm 0.161\, M_J$ and a radius of $1.024 \pm 0.092\, R_J$ yielding a mean density of $4.68^{+1.59}_{-0.99}$ g cm^{-3}. HAT-P-21b is a borderline object between the pM and pL class planets, and the transits occur near apastron. HAT-P-22b orbits the bright $V = 9.732$ G5 dwarf star HD 233731 on a circular orbit, with a period $P = 3.212220 \pm 0.000009$ days, transit epoch $T_c = 2454930.22001 \pm 0.00025$, and transit duration 0.1196 ± 0.0014 days. The host star has a mass of $0.92 \pm 0.03\, M_\odot$, radius of $1.04 \pm 0.04\, R_\odot$, effective temperature 5302 ± 80 K, and metallicity $[\mathrm{Fe/H}] = +0.24 \pm 0.08$. The planet has a mass of $2.147 \pm 0.061\, M_J$ and a compact radius of $1.080 \pm 0.058\, R_J$ yielding a mean density of $2.11^{+0.40}_{-0.29}$ g cm^{-3}. The host star also harbors an M-dwarf companion at a wide separation. Finally, HAT-P-23b orbits the $V = 12.432$ G0 dwarf star GSC 1632-01396 on a close to circular orbit, with a period $P = 1.212884 \pm 0.000002$ days, transit epoch $T_c = 2454852.26464 \pm 0.00018$, and transit duration 0.0908 ± 0.0007 days. The host star has a mass of $1.13 \pm 0.04\, M_\odot$, radius of $1.20 \pm 0.07\, R_\odot$, effective temperature 5905 ± 80 K, and metallicity $[\mathrm{Fe/H}] = +0.15 \pm 0.04$. The planetary companion has a mass of $2.090 \pm 0.111\, M_J$ and a radius of $1.368 \pm 0.090\, R_J$ yielding a mean density of 1.01 ± 0.18 g cm^{-3}. HAT-P-23b is an inflated and massive hot Jupiter on a very short period orbit, and has one of the shortest characteristic infall times ($7.5^{+2.9}_{-1.8}$ Myr) before it gets engulfed by the star.

Key words: stars: individual (HAT-P-20, HAT-P-21, HAT-P-22, HAT-P-23) – techniques: photometric – techniques: spectroscopic

Online-only material: color figure, machine-readable tables

1. INTRODUCTION

The majority of the ∼130 confirmed transiting extrasolar planets (TEPs) have been found to lie in the 0.5–2.0 M_J mass range. The apparent drop in their mass distribution at ∼2 M_J has been noted by, e.g., Southworth et al. (2009), and by Torres et al. (2010). In the currently known sample, 75% of the TEPs have planetary mass $M_p < 2.0\, M_J$, and there appears to be a minor peak in their occurrence rate at $M_p \approx 2\, M_J$, which then sharply falls off toward higher masses.

Are there any biases present against discovering massive planets? Such planets tend to be less inflated, and theory dictates that their radii shrink as their mass increases toward the brown dwarf regime. According to Baraffe et al. (2010), this reversal of the M_p–R_p relation happens around $M_p \approx 2$–$3\, M_J$, and falls off as $R_p \propto M_p^{-1/8}$ (see, e.g., Fortney et al. 2010). The smaller radii for massive planets yield a minor bias against discovering them via the transit method, since they produce shallower transits. Very massive planets can perhaps induce stellar variability of their host stars (Shkolnik et al. 2009), somewhat decreasing the efficiency of detecting their shallow transits via simple algorithms that expect constant out-of-transit light curves. Also, the host stars of massive planets are typically more rapid rotators: the average $v \sin i$ for host stars with planets

* Based in part on observations obtained at the W. M. Keck Observatory, which is operated by the University of California and the California Institute of Technology. Keck time has been granted by NOAO and NASA.
[12] NSF Fellow.

$M_p < 2\,M_J$ is 3.7 m s^{-1} (with 4.1 m s^{-1} standard deviation around the mean), whereas the same values for the massive planet host stars are 10.1 m s^{-1}(with 10.8 m s^{-1} standard deviation around the mean).[13] Six of the seven fastest rotators all harbor planets more massive than $2\,M_J$. This presents a bias against discovering them either via radial velocity (RV) searches, which are more efficient around quiet non-rotating dwarfs, or via transit searches, where the targets may be discarded during the confirmation phase. Along the same lines, the large RV amplitude of the host star, as caused by the planetary companion, may even lead to erroneous rejection during the reconnaissance phase of candidate confirmation, since such systems resemble eclipsing binaries. Finally, there is a tendency that massive planets are more likely to be eccentric[14] (Southworth et al. 2009), meaning that they require more RV observations for proper mapping of their orbits, and thus leading to a slower announcement rate. On the other hand, a strong bias *for* detecting such planets—-compensating for most of the effects above—is the fact that the large RV amplitudes of the host stars are easier to detect, since they do not require internal precisions at the meters per second level (see HAT-P-2, where valuable data were contributed to the RV fit by modest precision instruments yielding ∼1 km s^{-1} precision; Bakos et al. 2007). Altogether, while there are minor biases against detecting massive transiting planets, their overall effect is likely mitigated by the strong bias in favor of their detection, and the drop in frequency at $\gtrsim 2\,M_J$ seems to be real.

Massive planets are important for many reasons. They provide very strong constraints on formation and migration theories, which need to explain the observed distribution of planetary system parameters in a wide range (Baraffe et al. 2008, 2010), from 0.01 M_J (Corot-7b; Queloz et al. 2009) to 26.4 M_J (Corot-3b; Deleuil et al. 2008). Heavy mass objects necessitate the inclusion of other physical mechanisms for formation and migration, such as planet–planet scattering (Chatterjee et al. 2008; Ford & Rasio 2008), and the Kozai mechanism (Fabrycky & Tremaine 2007). They are borderline objects between planets and brown dwarfs, and help us understand how these populations differ and overlap (see Leconte et al. 2009 for a review). For example, a traditional definition of planets is that they have no deuterium burning, where the deuterium-burning limit is thought to be around 13 M_J (Spiegel et al. 2011). However, there are large uncertainties on this limit due to the numerous model parameters and solutions, and the fact that deuterium may be able to burn in the H/He layers above the core (Baraffe et al. 2008). Another possible definition of planets is based on their formation scenario, i.e., they are formed by accretion in a protoplanetary disk around their young host star, as opposed to the gravitational collapse of a molecular cloud (brown dwarfs).[15]

Perhaps related to the formation and migration mechanisms, a number of interesting correlations involving massive planets have been pointed out. Udry et al. (2002) noted that short-period massive planets are predominantly found in binary stellar systems. Southworth et al. (2009) noted that only 8.6% of the low-mass planets show significantly eccentric orbits, whereas 77% of the massive planets have eccentric orbits (although low-mass systems have lower signal-to-noise ratio (S/N) RV curves, rendering the detection of eccentric orbits more difficult). Curiously, there appears to be a lack of correlation between planetary mass and host star metallicity, while one would naively think that the formation of high-mass planets (via core accretion) would require higher metal content. Until this work, there was a hint of a correlation between planetary and stellar mass (e.g., Deleuil et al. 2008), in the sense that the most massive planets orbited $M_\star \gtrsim 1.2\,M_\odot$ stars, and there was a (biased) tendency that lower mass planets orbit less massive stars.

All of these observations suffer from small-number statistics and heavy biases. One way of improving our knowledge is to expand the sample of well-characterized planets. In this work we report on four new massive transiting planets around bright stars. This extends the currently known sample of bright ($V < 13.5$) and massive ($M_p > 2\,M_J$) transiting planets by 30% (from 13 to 17).[16] These discoveries were made by the Hungarian-made Automated Telescope Network (HATNet; Bakos et al. 2004) survey. HATNet has been one of the main contributors to the discovery of TEPs, among others such as the ground-based SuperWASP (Pollacco et al. 2006), TrES (Alonso et al. 2004), and XO projects (McCullough et al. 2005), and space-borne searches such as *CoRoT* (Baglin et al. 2006) and *Kepler* (Borucki et al. 2010). In operation since 2003, HATNet has now covered approximately 14% of the sky, searching for TEPs around bright stars ($8 \lesssim I \lesssim 14$). We operate six wide-field instruments: four at the Fred Lawrence Whipple Observatory (FLWO) in Arizona and two on the roof of the hangar servicing the Smithsonian Astrophysical Observatory's Submillimeter Array, in Hawaii.

The layout of this paper is as follows. In Section 2 we report the detections of the photometric signals and the follow-up spectroscopic and photometric observations for each of the planets. In Section 3 we describe the analysis of the data, beginning with the determination of the stellar parameters, continuing with a discussion of the methods used to rule out non-planetary, false positive scenarios which could mimic the photometric and spectroscopic observations, and finishing with a description of our global modeling of the photometry and RVs. Our findings are discussed in Section 4.

2. OBSERVATIONS

2.1. Photometric Detection

Table 1 summarizes the HATNet discovery observations of each new planetary system. The calibration of the HATNet frames was carried out using standard procedures correcting for the CCD bias, dark current, and flat-field structure. The calibrated images were then subjected to star detection and astrometry, as described in Pál & Bakos (2006). Aperture photometry was performed on each image at the stellar centroids derived from the Two Micron All Sky Survey (2MASS; Skrutskie et al. 2006) catalog and the individual astrometric solutions. For certain data sets (HAT-P-20, HAT-P-22, HAT-P-23) we also carried out an image subtraction (Alard 2000) based photometric reduction using discrete kernels (Bramich 2008), as described in Pál (2009b). The resulting light curves were decorrelated (cleaned of trends) using the External Parameter Decorrelation (EPD; see Bakos et al. 2010) technique in "constant" mode and the Trend Filtering Algorithm (TFA; see Kovács et al. 2005). The light curves were searched for periodic box-shaped signals using the Box Least-squares (BLS; see Kovács et al. 2002) method. Candidates were passed through a number of automatic filters to reject false alarms and obvious eclipsing binaries or other variable stars (two examples include checking for differences

[13] This includes those four planets announced in this paper.

[14] See, e.g., http://exoplanets.org for statistics.

[15] Note that the recent definition adopted by the exoplanet encyclopedia is 25 M_J (Schneider et al. 2011).

[16] Since the submission of this paper, the sample of massive transiting planets has further increased to ∼30.

Table 1
Summary of Photometric Observations

Instrument/Field	Date (s)	Number of Images	Median FWHM of PSF ($''$)	Cadence (s)	Filter
HAT-P-20					
HAT-7/G267	2007 Dec–2008 May	802	32.8	330	R
HAT-8/G267	2007 Oct–2008 May	1850	25.3	330	R
FLWO12/KeplerCam	2009 Mar 11	268	3.5	43	Sloan i
FLWO12/KeplerCam	2009 Oct 21	343	3.5	32	Sloan i
HAT-P-21					
HAT-6/G183	2006 Dec–2007 May	4528	37.1	330	I
HAT-9/G183	2006 Nov–2007 Jun	4586	40.5	330	I
HAT-5/G184	2006 Dec–2007 Jun	4040	36.0	330	I
HAT-8/G184	2006 Dec–2007 Jun	5606	40.5	330	I
HAT-6/G141	2008 Jan–2008 Jun	5142	25.9	330	R
HAT-9/G141	2008 Jan–2008 Jun	3964	27.5	330	R
FLWO12/KeplerCam	2009 Apr 20	243	3.9	53	Sloan i
FLWO12/KeplerCam	2010 Feb 15	412	4.8	43	Sloan i
LCOGT/FTN[a]	2010 Feb 19	511	3.0	31	Sloan i
HAT-P-22					
HAT-5/G139	2007 Dec–2008 May	4288	27.7	330	R
FLWO12/KeplerCam	2009 Feb 28	532	3.4	28	Sloan z
FLWO12/KeplerCam	2009 Apr 30	353	3.8	33	Sloan g
HAT-P-23					
HAT-6/G341	2007 Sep–2007 Dec	1178	24.7	330	R
HAT-9/G341	2007 Sep–2007 Nov	2351	27.7	330	R
FLWO12/KeplerCam	2008 Jun 14	147	3.0	73	Sloan i
FLWO12/KeplerCam	2008 Sep 8	246	3.6	73	Sloan i
FLWO12/KeplerCam	2008 Sep 13	265	3.2	73	Sloan i
FLWO12/KeplerCam	2008 Nov 3	117	3.3	89	Sloan i
FLWO12/KeplerCam	2009 Apr 19	46	4.6	150	Sloan g
FLWO12/KeplerCam	2009 Jul 13	150	4.1	73	Sloan i

Note. [a] Observations were performed without guiding due to a technical problem with the guiding system, and resulted in decreased data quality.

between the depths of even and odd transits when the period is doubled, and checking for evidence of a secondary eclipse at the period of the transit), and then passed a by-eye selection procedure which primarily rejects obvious blends with nearby eclipsing binaries or cases where the candidate selection is due to an artifact which is not captured by one of the automated filters. We detected significant signals in the light curves of the stars as summarized below.

1. *HAT-P-20*—GSC 1910-00239 (also known as 2MASS 07273995+2420118; $\alpha = 07^{\mathrm{h}}27^{\mathrm{m}}39\overset{\mathrm{s}}{.}96$, $\delta = +24^\circ20'11\overset{''}{.}9$; J2000; $V = 11.339$). A signal was detected for this star with an apparent depth of $\sim$10.8 mmag, and a period of $P = 2.8753$ days (see Figure 1). Note that the apparent HATNet depth stated here is attenuated by the presence of the fainter neighbor star that is not resolved on the coarse resolution ($9\overset{''}{.}5$ pixel^{-1}) HATNet pixels. Also, the depth by fitting a trapezoid instead of the correct Mandel & Agol (2002) model is somewhat shallower than the maximum depth in the Mandel & Agol (2002) model fit (which was 19.6 mmag; see later in Section 3.3). Note that the dilution in the HATNet light curve is accounted for by the dilution factor parameter included in the global fitting procedure described in Section 3.3. The follow-up light curves discussed in Section 2.4 are obtained with instruments that have much higher spatial resolution, and when necessary are reduced using the image subtraction technique, so that they are not affected by dilution from any known neighbors. The drop in brightness had a first-to-last-contact duration, relative to the total period, of $q = 0.0268 \pm 0.0003$, corresponding to a total duration of $Pq = 1.848 \pm 0.019$ hr. HAT-P-20 has a red companion (2MASS 07273963+2420171, $J - K = 0.92$) at $6\overset{''}{.}86$ separation that is fainter than HAT-P-20 by $\Delta R = 1.36$ mag.
2. *HAT-P-21*—GSC 3013-01229 (also known as 2MASS 11250598+4101406; $\alpha = 11^{\mathrm{h}}25^{\mathrm{m}}05\overset{\mathrm{s}}{.}88$, $\delta = +41^\circ01'40\overset{''}{.}6$; J2000; $V = 11.685$). A signal was detected for this star with an apparent depth of $\sim$8.0 mmag, and a period of $P = 4.1245$ days (see Figure 2). The drop in brightness had a first-to-last-contact duration, relative to the total period, of $q = 0.0371 \pm 0.0007$, corresponding to a total duration of $Pq = 3.672 \pm 0.065$ hr.
3. *HAT-P-22*—HD 233731 (also known as GSC 03441-00925 and 2MASS 10224361+5007420; $\alpha = 10^{\mathrm{h}}22^{\mathrm{m}}43\overset{\mathrm{s}}{.}68$, $\delta = +50^\circ07'42\overset{''}{.}0$; J2000; $V = 9.732$). A signal was detected for this star with an apparent depth of $\sim$9.7 mmag, and a period of $P = 3.2122$ days (see Figure 3). The drop in brightness had a first-to-last-contact duration, relative to the total period, of $q = 0.0372 \pm 0.0004$, corresponding to a total duration of $Pq = 2.869 \pm 0.033$ hr. HAT-P-22 has a close red companion star (2MASS 10224397+5007504, $J - K = 0.86$) at $9\overset{''}{.}1$ separation and $\Delta i = 2.58$ mag fainter.
4. *HAT-P-23*—GSC 1632-01396 (also known as 2MASS 20242972+1645437; $\alpha = 20^{\mathrm{h}}24^{\mathrm{m}}29\overset{\mathrm{s}}{.}88$, $\delta = +16^\circ45'43\overset{''}{.}7$; J2000; $V = 12.432$). A signal was detected for this star with an apparent depth of $\sim$11.5 mmag, and a period of $P = 1.2129$ days (see Figure 4). Similarly to HAT-P-20, the depth was attenuated by close-by faint neighbors. The drop in brightness had a first-to-last-contact duration, relative to

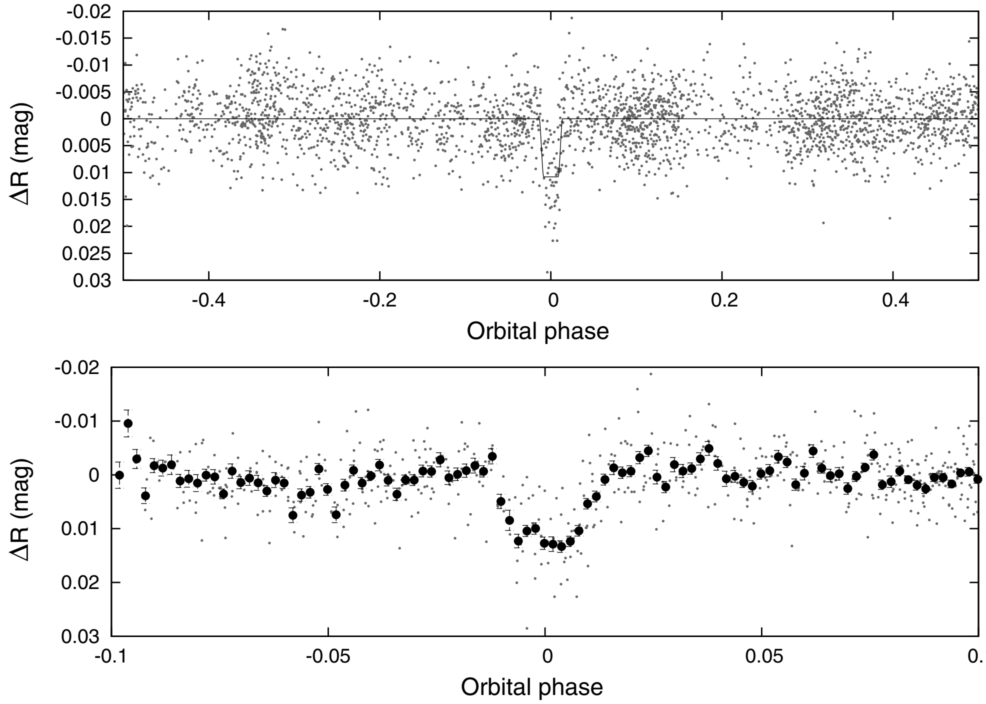

Figure 1. Unbinned light curve of HAT-P-20 including all 2600 instrumental R-band 5.5 minute cadence measurements obtained with the HAT-7 and HAT-8 telescopes of HATNet (see Table 1 for details), and folded with the period $P = 2.8753172$ days resulting from the global fit described in Section 3. The solid line shows the "P1P3" transit model fit to the light curve (Section 3.3). The bold points in the lower panel show the light curve binned in phase with a bin size of 0.002.

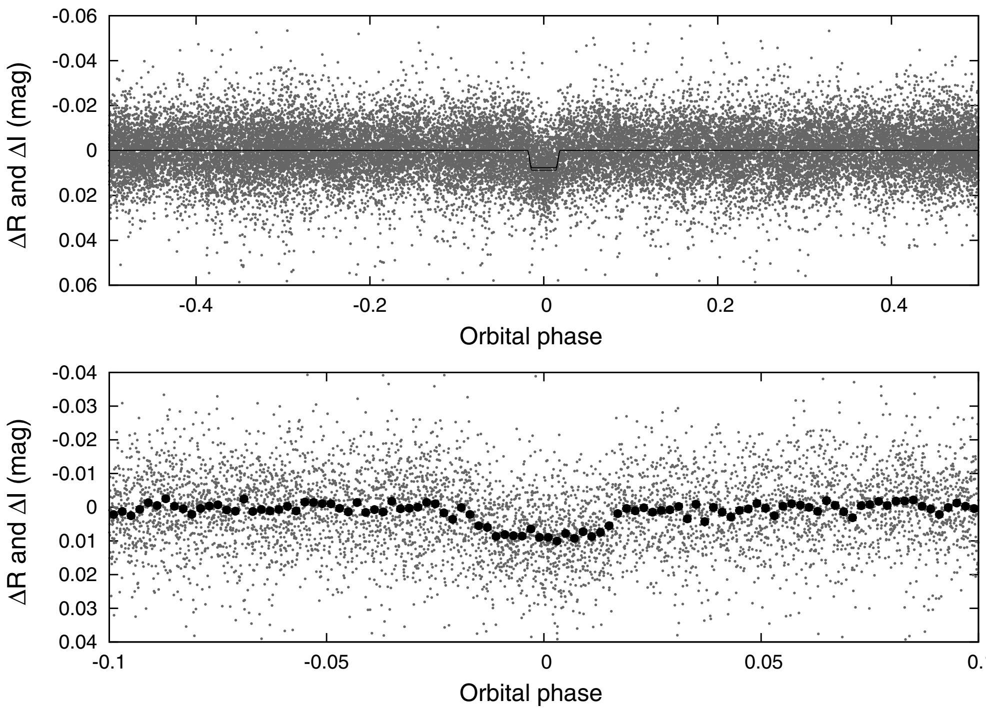

Figure 2. Unbinned light curve of HAT-P-21 including all 28,000 instrumental I-band and R-band 5.5 minute cadence measurements obtained with the HAT-5, HAT-6, HAT-8, and HAT-9 telescopes of HATNet (see Table 1 for details), and folded with the period $P = 4.1244808$ days resulting from the global fit described in Section 3. The solid line shows the "P1P3" transit model fit to the light curve (Section 3.3). The bold points in the lower panel show the light curve binned in phase with a bin size of 0.002.

the total period, of $q = 0.0748 \pm 0.0006$, corresponding to a total duration of $Pq = 2.178 \pm 0.017$ hr.

2.2. Reconnaissance Spectroscopy

As is routine in the HATNet project, all candidates are subjected to careful scrutiny before investing valuable time on large telescopes. This includes spectroscopic observations at relatively modest facilities to establish whether the transit-like feature in the light curve of a candidate might be due to astrophysical phenomena other than a planet transiting a star. Many of these false positives are associated with large RV variations in the star (tens of kilometers per second)

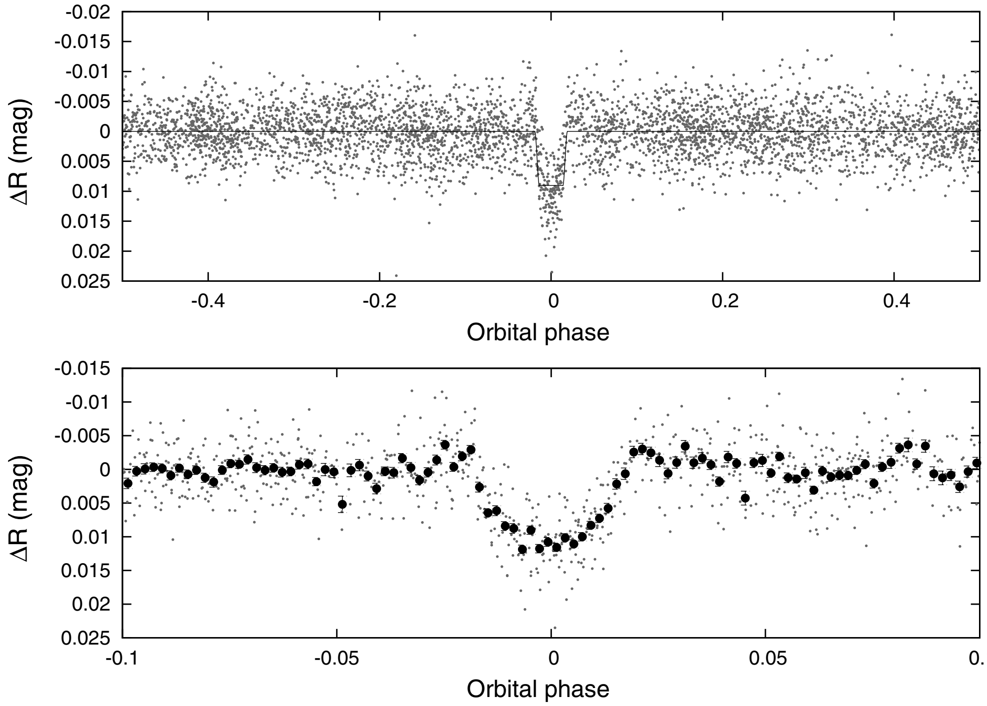

Figure 3. Unbinned light curve of HAT-P-22 including all 4200 instrumental R-band 5.5 minute cadence measurements obtained with the HAT-5 telescope of HATNet (see the text for details), and folded with the period $P = 3.2122198$ days resulting from the global fit described in Section 3. The solid line shows the "P1P3" transit model fit to the light curve (Section 3.3). The bold points in the lower panel show the light curve binned in phase with a bin size of 0.002.

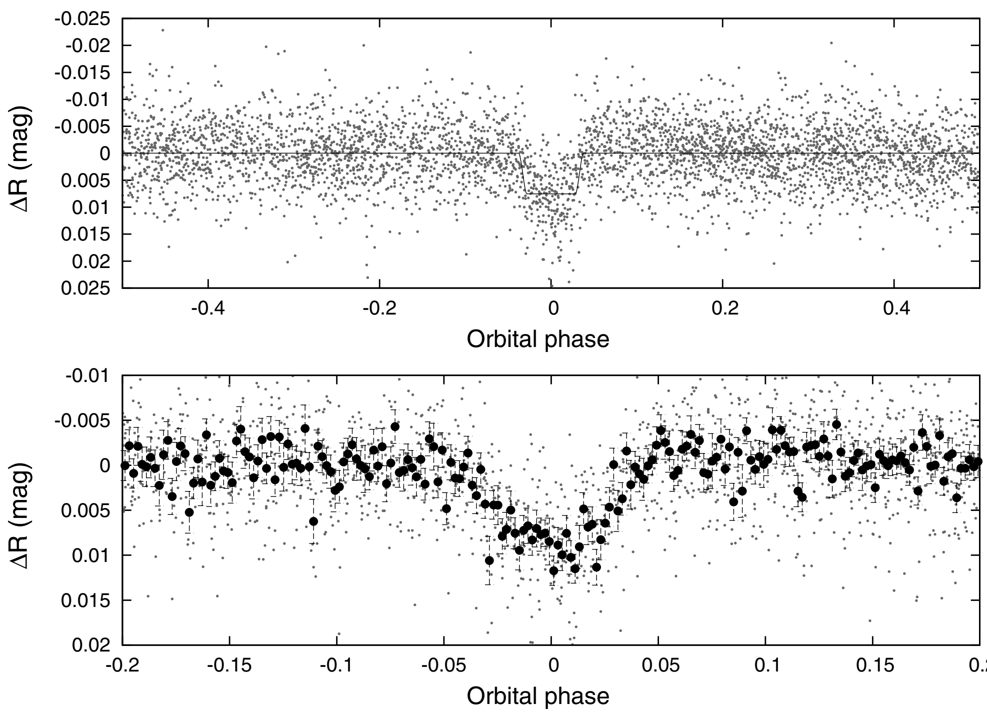

Figure 4. Unbinned light curve of HAT-P-23 including all 3500 instrumental R-band 5.5 minute cadence measurements obtained with the HAT-6 and HAT-9 telescopes of HATNet (see Table 1 for details), and folded with the period $P = 1.2128841$ days resulting from the global fit described in Section 3. The solid line shows the "P1P3" transit model fit to the light curve (Section 3.3). The bold points in the lower panel show the light curve binned in phase with a bin size of 0.002.

that are easily recognized. The reconnaissance spectroscopic observations and results for each system are summarized in Table 2; below we provide a brief description of the instruments used, the data reduction, and the analysis procedure.

One of the tools we have used for this purpose is the Harvard-Smithsonian Center for Astrophysics (CfA) Digital Speedometer (DS; Latham 1992), an echelle spectrograph mounted on the FLWO 1.5 m telescope. This instrument delivers high-resolution spectra ($\lambda/\Delta\lambda \approx 35{,}000$) over a single order centered on the Mg I b triplet (∼5187 Å), with typically low S/Ns that are nevertheless sufficient to derive RVs with moderate precisions of 0.5–1.0 km s^{-1} for slowly rotating stars. The

Table 2
Summary of Reconnaissance Spectroscopy Observations

Instrument	Date(s)	Number of Spectra	$T_{\mathrm{eff}\star}$ (K)	$\log g_\star$ (cgs)	$v \sin i$ (km s^{-1})	γ_{RV}[a] (km s^{-1})
HAT-P-20						
DS	2009 Feb 11–2009 Feb 15	3	4500 ± 125	4.0 ± 0.25	$0\pm^{4}_{0}$	−18.81 ± 0.68
FIES	2009 Oct 7	1	4500	4.0	4	−16.76 ± 0.1
HAT-P-21						
DS	2009 Mar 8–2009 Apr 5	3	5750 ± 125	4.5 ± 0.25	3.0 ± 3.0	−53.19 ± 0.09
HAT-P-22						
DS	2009 Feb 11–2009 Feb 16	4	5250 ± 125	4.5 ± 0.25	2.0 ± 2.0	+12.49 ± 0.28
HAT-P-23						
DS	2008 May 19–2008 Sep 14	5	6000 ± 125	4.5 ± 0.25	9.0 ± 1.0	−15.10 ± 0.30

Note. [a] The mean heliocentric RV of the target (in the IAU system). For the DS observations, the error gives the rms of the individual velocity measures for the target. For the FIES observation this is the estimated uncertainty on the individual measurement.

Table 3
Summary of High-resolution/High-S/N Spectroscopic Observations

Instrument	Date(s)	Number of RV Obs.
HAT-P-20		
Keck/HIRES	2009 Apr–2009 Dec	10
HAT-P-21		
Keck/HIRES	2009 May–2010 Feb	15
HAT-P-22		
Keck/HIRES	2009 Apr–2009 Dec	12
HAT-P-23		
Keck/HIRES	2008 Jun–2009 Dec	13

same spectra can be used to estimate the effective temperature, surface gravity, and projected rotational velocity of the host star, as described by Torres et al. (2002). With this facility we are able to reject many types of false positives, such as F dwarfs orbited by M dwarfs, grazing eclipsing binaries, and many triple or quadruple star systems. Additional tests are performed with other spectroscopic material described in the next section.

Another of the tools we have used for this purpose is the Fiber-fed Échelle Spectrograph (FIES) at the 2.5 m Nordic Optical Telescope (NOT) at La Palma, Spain (Djupvik & Andersen 2010). We used the medium-resolution fiber which produces spectra at a resolution of $\lambda/\Delta\lambda \approx 46{,}000$ and a wavelength coverage of ~3600–7400 Å to observe HAT-P-20. The spectrum was extracted and analyzed to measure the RV, effective temperature, surface gravity, and projected rotation velocity of the host star, following the procedures described by Buchhave et al. (2010).

Based on the observations summarized in Table 2, we find that HAT-P-21, HAT-P-22, and HAT-P-23 have rms residuals consistent with no detectable RV variation within the precision of the measurements. The reconnaissance observations of HAT-P-20 hinted at a $K \sim 1$ km s^{-1} orbital variation roughly in phase with the photometric ephemeris (these velocities are consistent with the $K \sim 1.2$ km s^{-1} orbit of HAT-P-20 measured subsequently with Keck/HIRES given the ~0.5 km s^{-1} precision of the DS). All spectra were single-lined, i.e., there is no evidence that any of these targets consist of more than one star. The gravities for all of the stars indicate that they are dwarfs.

2.3. High-resolution, High-S/N Spectroscopy

We proceeded with the follow-up of each candidate by obtaining high-resolution, high-S/N spectra to characterize the RV variations, and to refine the determination of the stellar parameters. These observations are summarized in Table 3. The RV measurements and uncertainties are given in Tables 4–7 for HAT-P-20–HAT-P-23, respectively. The period-folded data, along with our best fits described below in Section 3, are displayed in Figures 6–9 for HAT-P-20–HAT-P-23. Below we briefly describe the instruments used, the data reduction, and the analysis procedure.

Observations were made of all four planet host stars with the HIRES instrument (Vogt et al. 1994) on the Keck I telescope located on Mauna Kea, Hawaii. The width of the spectrometer slit was 0.″86, resulting in a resolving power of $\lambda/\Delta\lambda \approx 55{,}000$, with a wavelength coverage of ~3800–8000 Å. We typically used the B5 decker yielding a 3.″5(H) × 0.″861(W) slit, and for the last few observations on each target we used the C2 decker that enables a better sky subtraction due to the longer slit 14.″0(H) × 0.″861(W). The slit height was oriented with altitude (vertical), except for rare cases, when the slit would

Table 4
Relative Radial Velocities, Bisector Spans, and Activity Index Measurements of HAT-P-20

$\mathrm{BJD_{UTC}}$[a] (2,454,000 +)	RV[b] (m s^{-1})	σ_{RV}[c] (m s^{-1})	BS (m s^{-1})	σ_{BS} (m s^{-1})	S[d]	σ_S
934.84149 . . .	−1139.51	2.94	. . .	. . .	. . .	. . .
954.82485 . . .	. . .	. . .	−8.00	3.22	2.051	0.075
954.83175 . . .	−942.88	2.24	−18.65	8.02	2.900	0.035
956.80481 . . .	1092.32	2.28	−42.21	10.81	3.305	0.018
983.73851 . . .	−1151.02	2.39	18.53	4.51	2.853	0.016
984.74064 . . .	328.09	2.14	6.85	6.11	2.879	0.016
986.74296 . . .	−1225.77	2.34	15.28	7.78	2.588	0.029
1107.15226 .	−870.02	4.89	10.00	17.65	1.352	0.043
1109.05752 .	1233.55	3.76	−1.23	7.66	2.783	0.018
1191.10274 .	−1147.72	2.07	14.55	6.16	3.412	0.016
1192.11754 .	1100.72	2.12	4.88	2.83	3.346	0.015

Notes. Note that for the iodine-free template exposures we do not measure the RV but do measure the BS and S index. Such template exposures can be distinguished by the missing RV value.
[a] Barycentric Julian dates throughout the paper are calculated from Coordinated Universal Time (UTC).
[b] The zero-point of these velocities is arbitrary. An overall offset γ_{rel} fitted to these velocities in Section 3.3 has *not* been subtracted.
[c] Internal errors excluding the component of astrophysical jitter considered in Section 3.3.
[d] Relative chromospheric activity index, not calibrated to the scale of Vaughan et al. (1978).

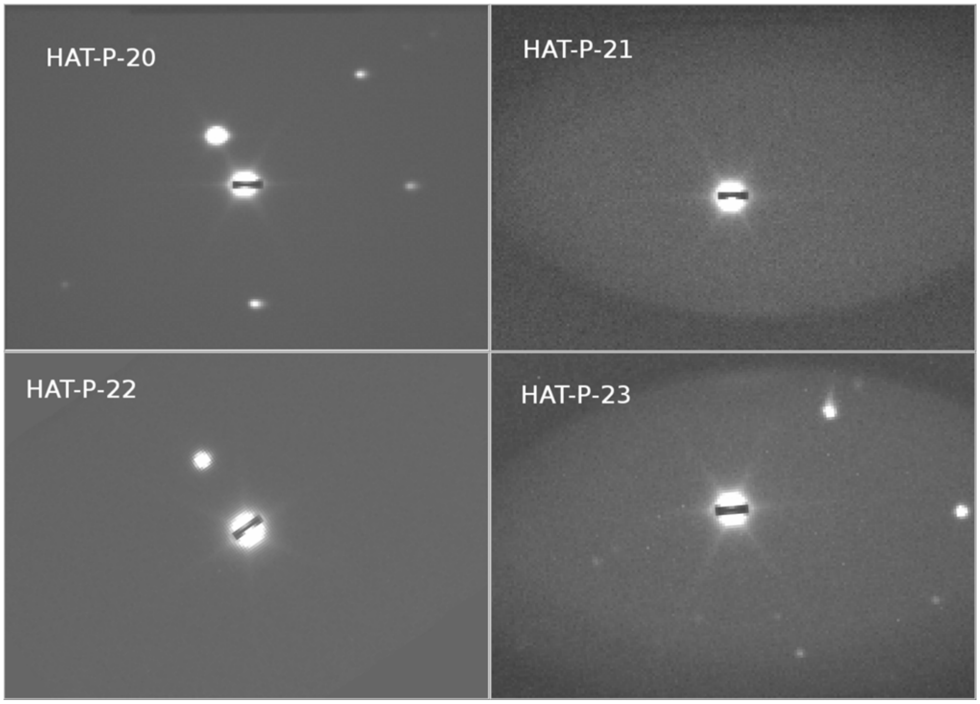

Figure 5. Keck/HIRES guider camera snapshots of HAT-P-20–HAT-P-23 (labeled). North is up and east is to the left. The snapshots cover an area of approximately 30″ × 20″. The slit is also visible, as positioned on the planet host stars.

Table 5
Relative Radial Velocities, Bisector Spans, and Activity Index Measurements of HAT-P-21

BJD_{UTC} (2,454,000 +)	RV ($m\,s^{-1}$)	σ_{RV} ($m\,s^{-1}$)	BS ($m\,s^{-1}$)	σ_{BS} ($m\,s^{-1}$)	S	σ_S
954.91548 . . .	. . .	. . .	3.67	5.10	0.819	0.002
954.92307 . . .	221.51	2.88	−9.60	13.62	0.829	0.003
955.86532 . . .	−274.01	2.48	−8.08	5.81	0.823	0.003
955.98849 . . .	−314.29	2.76	7.51	12.62	0.855	0.005
957.00006 . . .	−378.18	3.00	2.88	8.36	0.866	0.009
963.95573 . . .	−197.70	2.68	−12.46	5.48	0.789	0.003
983.85638 . . .	212.70	2.72	−4.61	3.33	0.815	0.003
985.87988 . . .	−406.23	2.46	5.88	4.95	0.809	0.003
986.85645 . . .	509.76	3.01	−0.70	7.24	0.803	0.005
987.86480 . . .	270.66	2.92	−6.96	4.20	0.810	0.004
1174.14589 .	−145.85	3.13	0.01	6.54	0.833	0.005
1191.14119 .	−391.67	2.75	5.76	5.16	0.832	0.005
1192.12302 .	−457.57	2.67	7.04	3.15	0.809	0.005
1193.11001 .	496.07	2.58	2.50	3.85	0.794	0.005
1197.15057 .	459.61	2.59	9.69	4.91	0.777	0.005
1229.12322 .	−469.62	2.81	−2.53	5.81	0.821	0.005

Note. Same as those of Table 4.

Table 6
Relative Radial Velocities, Bisector Spans, and Activity Index Measurements of HAT-P-22

BJD_{UTC} (2,454,000 +)	RV ($m\,s^{-1}$)	σ_{RV} ($m\,s^{-1}$)	BS ($m\,s^{-1}$)	σ_{BS} ($m\,s^{-1}$)	S	σ_S
928.94934 . . .	187.55	1.12	13.71	4.73	0.557	0.002
954.88137 . . .	284.38	1.12	7.07	3.69	0.556	0.002
954.88605 . . .	. . .	. . .	−2.17	3.34	0.554	0.001
955.79962 . . .	77.44	1.46	6.00	13.88	0.533	0.008
956.96383 . . .	−273.80	1.30	4.41	10.92	0.531	0.005
963.92157 . . .	−14.63	1.33	−0.17	6.57	0.570	0.002
983.82710 . . .	282.58	0.98	2.20	3.79	0.572	0.003
985.81064 . . .	−298.55	1.14	−2.81	2.96	0.560	0.002
986.84124 . . .	239.74	1.39	−7.48	6.58	0.553	0.003
988.83025 . . .	−300.15	1.31	−16.80	8.24	0.555	0.002
1191.14866 .	−326.24	1.32	−0.33	5.00	0.843	0.003
1193.10170 .	255.62	1.30	−8.71	6.79	0.835	0.003
1193.93435 .	−192.43	1.38	5.08	5.27	0.843	0.004

Note. Same as those of Table 4.

have run through the faint companion to HAT-P-20 or HAT-P-22. A Keck/HIRES snapshot for each planet host star is shown in Figure 5. Spectra were obtained through an iodine gas absorption cell, which was used to superimpose a dense forest of I_2 lines on the stellar spectrum and establish an accurate wavelength fiducial (see Marcy & Butler 1992). For each target an additional exposure was taken without the iodine cell, for use as a template in the reductions. Relative RVs in the solar system barycentric frame were derived as described by Butler et al. (1996), incorporating full modeling of the spatial and temporal variations of the instrumental profile.

In each of Figures 6–9 we show also the relative S index, which is a measure of the chromospheric activity of the star derived from the flux in the cores of the Ca II H and K lines. This index was computed following the prescription given by Vaughan et al. (1978), and as described in Hartman et al. (2009). Note that our relative S index has not been calibrated to the scale of Vaughan et al. (1978). We do not detect any significant variation of the index correlated with orbital phase; such a correlation might have indicated that the RV variations could be due to stellar activity, casting doubt on the planetary nature of the candidate.

2.4. Photometric Follow-up Observations

In order to permit a more accurate modeling of the light curves, we conducted additional photometric observations with the KeplerCam CCD camera on the FLWO 1.2 m telescope for each star, and with the Faulkes North Telescope (FTN) of the Las Cumbres Observatory Global Network (LCOGT) at

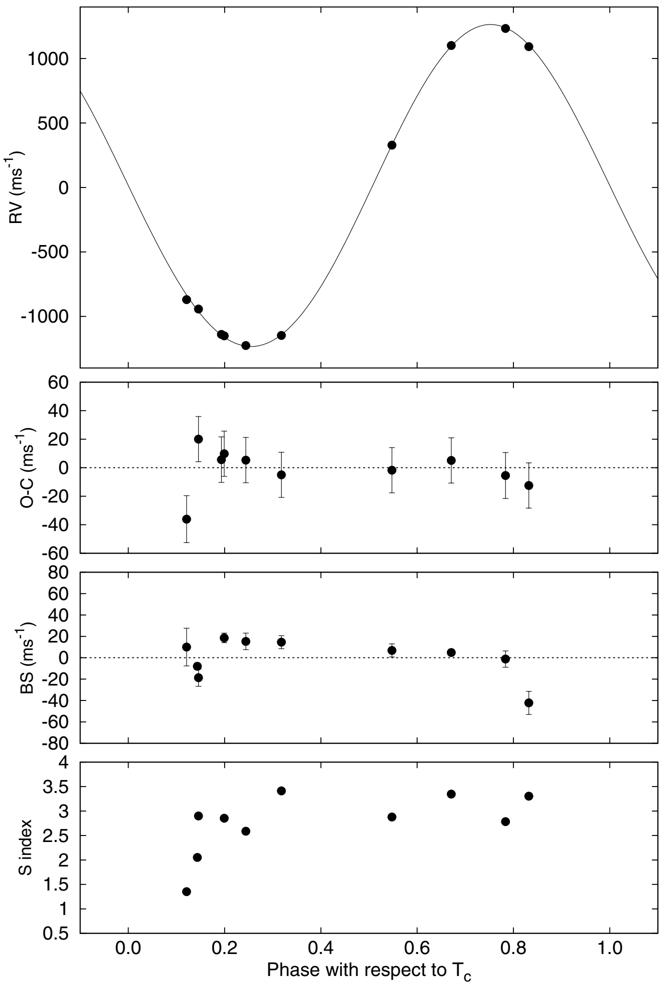

Figure 6. Top panel: Keck/HIRES RV measurements for HAT-P-20 shown as a function of orbital phase, along with our best-fit eccentric model (see Table 14). Zero phase corresponds to the time of mid-transit. The center-of-mass velocity has been subtracted. The rms around the best orbital fit is 16.2 m s^{-1}. Second panel: velocity $O-C$ residuals from the best fit. The error bars for both the top and second panels include a component from the jitter (15.7 m s^{-1}) added in quadrature to the formal errors (see Section 3.3). Third panel: bisector spans (BS), with the mean value subtracted. The measurement from the template spectrum is included (see Section 3.2). Bottom panel: relative chromospheric activity index S measured from the Keck spectra.

Table 7
Relative Radial Velocities, Bisector Spans, and Activity Index Measurements of HAT-P-23

$\mathrm{BJD_{UTC}}$ (2,454,000+)	RV (m s^{-1})	σ_{RV} (m s^{-1})	BS (m s^{-1})	σ_{BS} (m s^{-1})	S	σ_S
638.09243 ...	...	...	−4.89	4.59	1.170	0.020
638.10601 ...	−137.90	4.49	−0.45	5.22	0.797	0.006
674.91404 ...	374.64	5.15	−10.71	3.99	0.794	0.006
723.78719 ...	−209.16	5.55	−1.68	13.38	0.738	0.006
725.85309 ...	329.57	6.18	12.86	6.55	0.749	0.006
726.87976 ...	277.98	4.20	−26.82	6.17	0.770	0.005
727.76247 ...	−210.01	4.81	−35.11	5.18	0.811	0.006
727.89619 ...	−19.91	4.77	−30.29	5.05	0.795	0.005
777.82189 ...	214.73	4.54	−12.64	4.43	0.754	0.005
810.72960 ...	290.22	5.63	−13.57	5.59	0.726	0.006
955.04676 ...	388.82	4.74	−15.76	3.57	0.761	0.006
985.99494 ...	−369.93	4.42	−19.69	5.06	0.718	0.006
1192.70812 .	348.01	4.40	−14.40	4.53	0.726	0.005
1193.71080 .	83.68	4.57	−20.67	4.23	0.825	0.008

Notes. Same as those of Table 4.

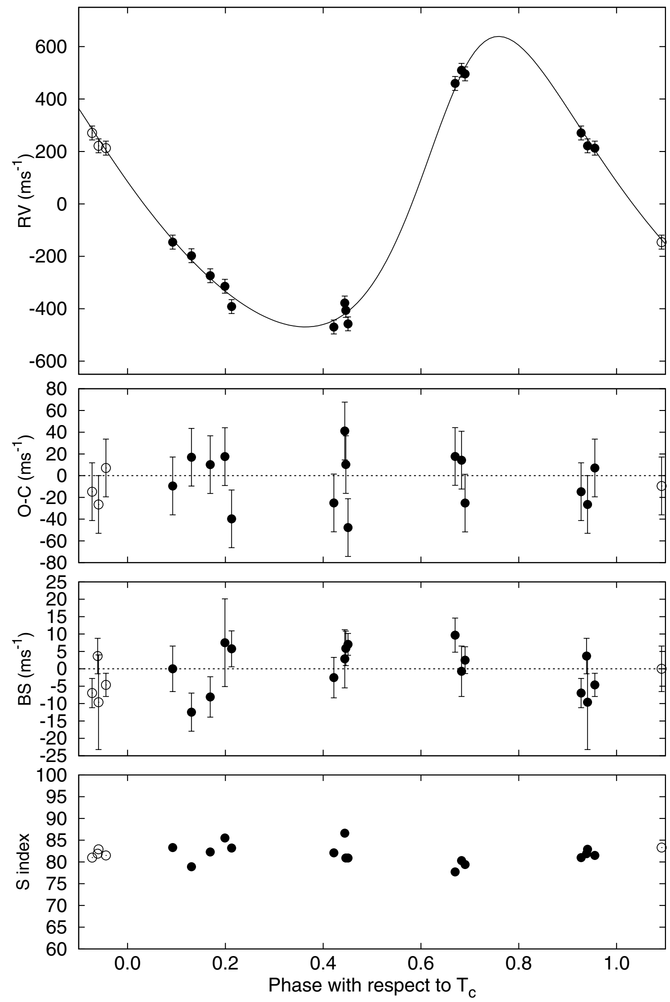

Figure 7. Keck/HIRES observations of HAT-P-21. The panels are as in Figure 6. The parameters used in the best-fit model are given in Table 14, the RV jitter was 26.4 m s^{-1}, and the fit rms was 26.6 m s^{-1}. Observations shown twice are represented with open symbols.

Hawaii for HAT-P-21 only. The observations for each target are summarized in Table 1.

The reduction of these images, including basic calibration, astrometry, and aperture photometry, was performed as described by Bakos et al. (2010). In each case we obtained light curves for all stars in the 2MASS catalog within the field of view of the observations and confirm that the primary target is the source of the transit rather than one of the known neighboring stars. We found that the aperture photometry for HAT-P-20 was significantly affected by the close-by neighbor star 2MASS 07273995+2420118 with $\Delta i = 1.1$ mag difference at $6\farcs86$ separation (Figure 5). Thus, we performed image subtraction on the FLWO 1.2 m images with the same toolset used for the HATNet reductions, but applied a discrete kernel with half-size of 5 pixels and no spatial variations. Indeed, for this stellar configuration, the image subtraction results proved to be superior to the aperture photometry. For all of the follow-up light curves, we performed EPD and TFA to remove trends simultaneously with the light curve modeling (for more details, see Section 3, and Bakos et al. 2010). The final time series, together with our best-fit transit light curve model, are shown in the top portion of Figures 10–13; the individual measurements are reported in Tables 8–11, for HAT-P-20 through HAT-P-23, respectively.

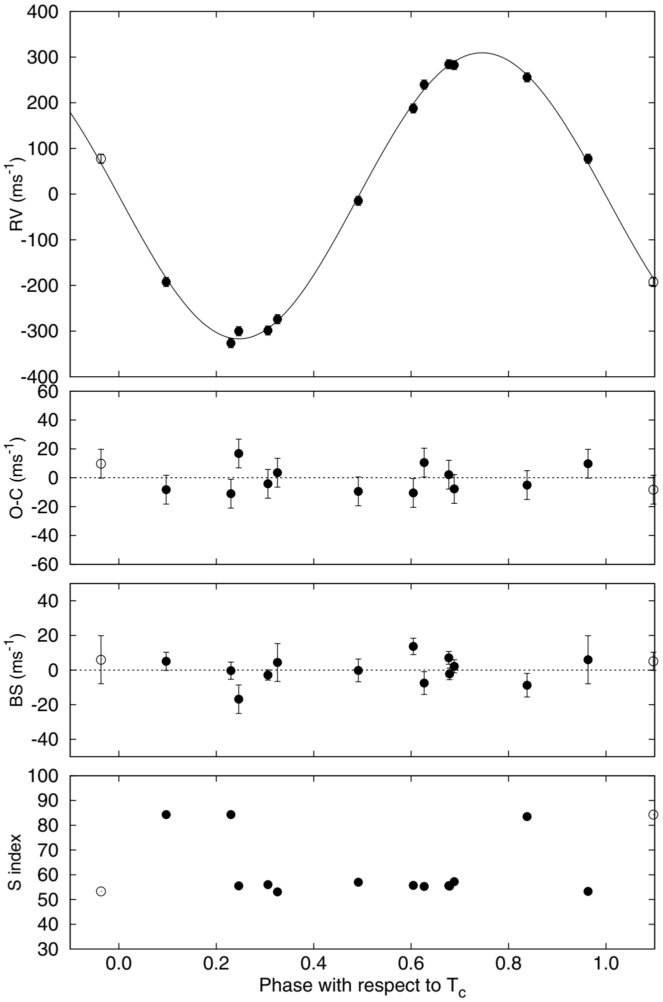

Figure 8. Keck/HIRES observations of HAT-P-22. The panels are as in Figure 6. The parameters used in the best-fit model are given in Table 14, the RV jitter was 9.9 m s^{-1}, and the fit rms was 10.0 m s^{-1}. Observations shown twice are represented with open symbols.

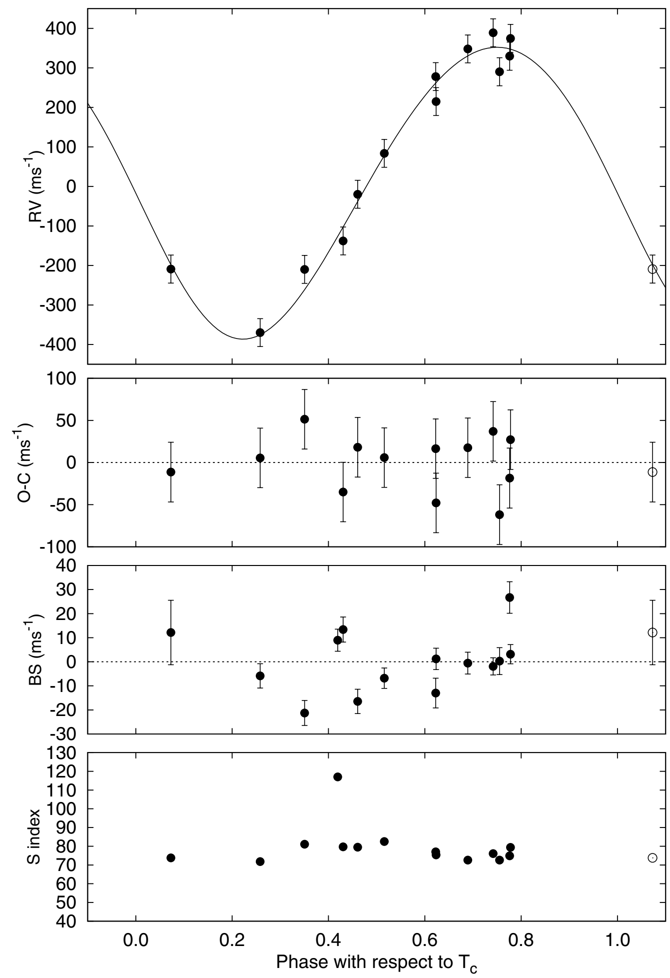

Figure 9. Keck/HIRES observations of HAT-P-23. The panels are as in Figure 6. The parameters used in the best-fit model are given in Table 14, and the RV jitter was 34.7 m s^{-1}. Observations shown twice are represented with open symbols.

Table 8
High-precision Differential Photometry of HAT-P-20

BJD_{UTC} (2,400,000 +)	Mag[a]	σ_{Mag}	Mag(orig)[b]	Filter
54902.59749	−0.00169	0.00075	10.66286	*i*
54902.59799	−0.00139	0.00075	10.66200	*i*
54902.59848	−0.00469	0.00075	10.65893	*i*
54902.59919	0.00281	0.00075	10.66596	*i*
54902.59970	−0.00108	0.00075	10.66316	*i*
54902.60020	0.00141	0.00075	10.66524	*i*
54902.60089	0.00440	0.00075	10.66726	*i*
54902.60139	0.00040	0.00075	10.66424	*i*
54902.60190	−0.00064	0.00075	10.66234	*i*
54902.60259	−0.00009	0.00075	10.66388	*i*

Notes.
[a] The out-of-transit level has been subtracted. These magnitudes have been subjected to the EPD and TFA procedures, carried out simultaneously with the transit fit.
[b] Raw magnitude values without application of the EPD and TFA procedures.

(This table is available in its entirety in a machine-readable form in the online journal. A portion is shown here for guidance regarding its form and content.)

Table 9
High-precision Differential Photometry of HAT-P-21

BJD_{UTC} (2,400,000 +)	Mag[a]	σ_{Mag}	Mag(orig)[b]	Filter
54942.76369	0.01133	0.00088	10.43700	*i*
54942.76432	0.01370	0.00088	10.43950	*i*
54942.76495	0.00989	0.00088	10.43550	*i*
54942.76574	0.00891	0.00088	10.43490	*i*
54942.76637	0.00974	0.00088	10.43570	*i*
54942.76698	0.01073	0.00088	10.43650	*i*
54942.76779	0.00961	0.00088	10.43480	*i*
54942.76839	0.00938	0.00088	10.43450	*i*
54942.76902	0.01249	0.00088	10.43800	*i*
54942.76980	0.01011	0.00088	10.43520	*i*

Note. Same as those of Table 8.

(This table is available in its entirety in a machine-readable form in the online journal. A portion is shown here for guidance regarding its form and content.)

3. ANALYSIS

3.1. Properties of the Parent Stars

Fundamental parameters for each of the host stars, including the mass ($M_\star$) and radius ($R_\star$), which are needed to infer the planetary properties, depend strongly on other stellar quantities that can be derived spectroscopically. For this we have relied on

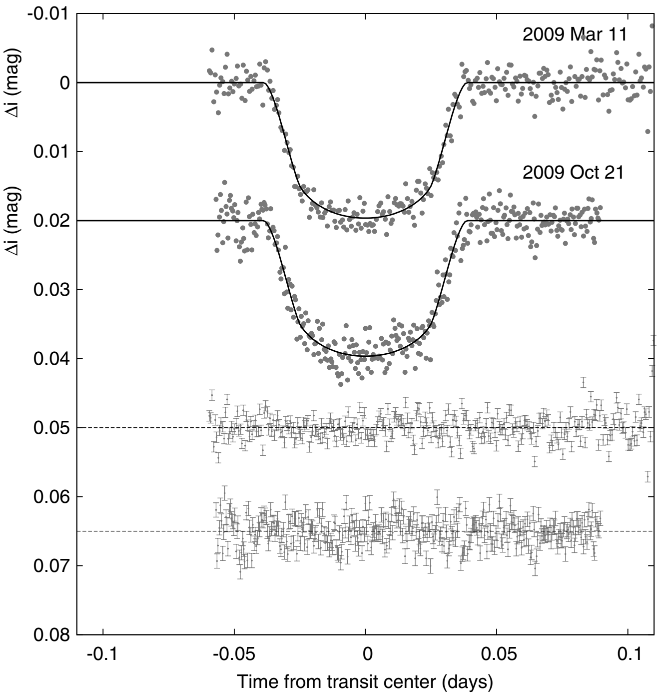

Figure 10. Unbinned transit light curves for HAT-P-20, acquired with KeplerCam at the FLWO 1.2 m telescope. The light curves have been EPD and TFA processed, as described in Section 3.3. The dates of the events are indicated. Curves after the first are displaced vertically for clarity. Our best fit from the global modeling described in Section 3.3 is shown by the solid lines. Residuals from the fits are displayed at the bottom, in the same order as the top curves. The error bars represent the photon and background shot noise, plus the readout noise.

Table 10
High-precision Differential Photometry of HAT-P-22

BJD_{UTC} (2,400,000 +)	Mag[a]	σ_{Mag}	Mag(orig)[b]	Filter
54891.60570	0.00028	0.00069	8.78803	z
54891.60603	−0.00100	0.00069	8.78658	z
54891.60636	−0.00189	0.00069	8.78541	z
54891.60667	−0.00138	0.00069	8.78514	z
54891.60702	−0.00237	0.00069	8.78534	z
54891.60735	0.00030	0.00069	8.78923	z
54891.60767	0.00404	0.00069	8.79234	z
54891.60801	−0.00170	0.00069	8.78696	z
54891.60831	0.00257	0.00069	8.79009	z
54891.60865	−0.00145	0.00069	8.78653	z

Notes. Same as those of Table 8.

(This table is available in its entirety in a machine-readable form in the online journal. A portion is shown here for guidance regarding its form and content.)

our template spectra obtained with the Keck/HIRES instrument, and the analysis package known as Spectroscopy Made Easy (SME; Valenti & Piskunov 1996), along with the atomic line database of Valenti & Fischer (2005). For each star, SME yielded the following initial values and uncertainties (which we have conservatively doubled for the temperature and metallicity to include our estimates of the systematic errors).

1. *HAT-P-20*—effective temperature $T_{\rm eff\star} = 4626 \pm 104$ K, stellar surface gravity $\log g_\star = 4.80 \pm 0.1$ (cgs), metallicity $[{\rm Fe/H}] = +0.31 \pm 0.08$ dex, and projected rotational velocity $v \sin i = 3.1 \pm 0.5$ km s^{-1}.

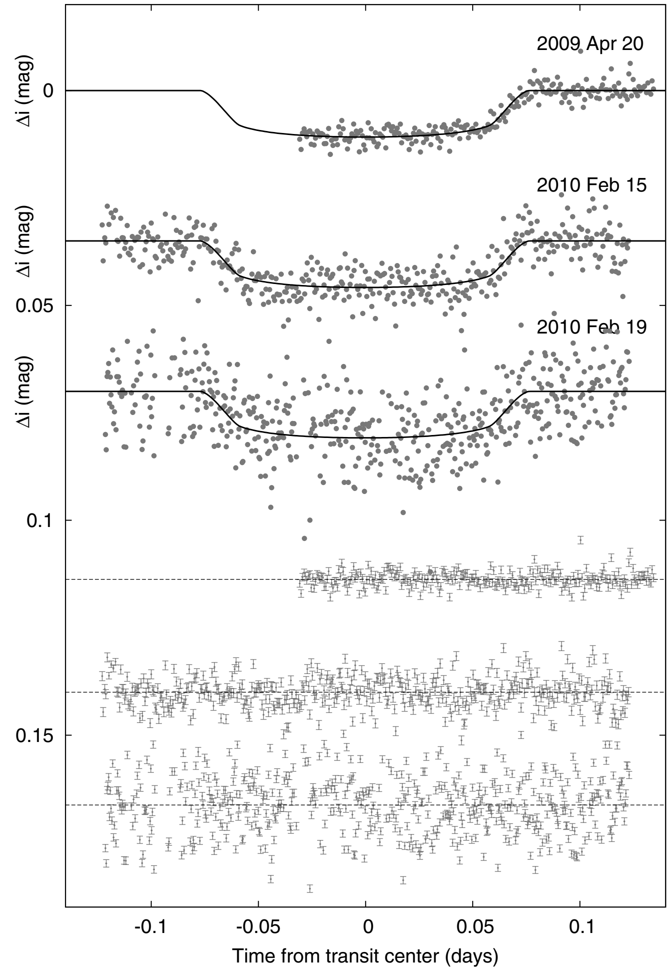

Figure 11. Similar to Figure 10; here we show the follow-up light curves for HAT-P-21.

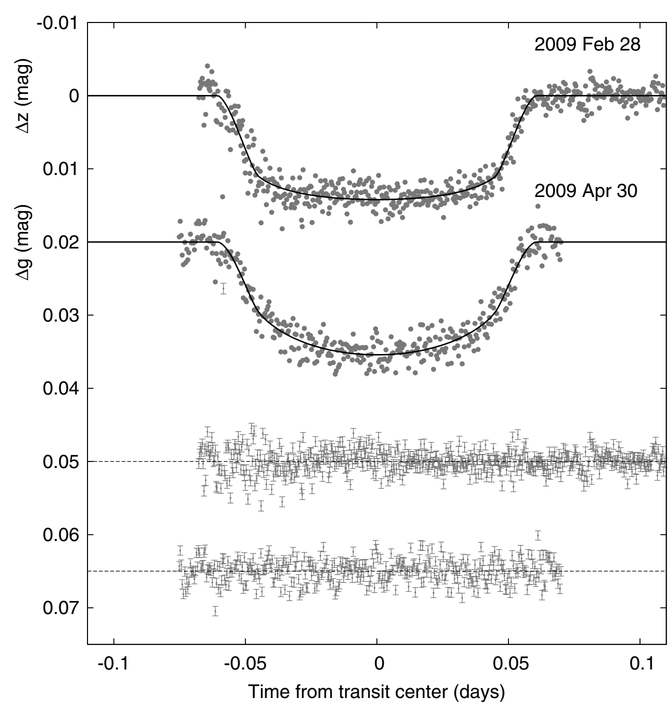

Figure 12. Similar to Figure 10; here we show the follow-up light curves for HAT-P-22.

Table 11
High-precision Differential Photometry of HAT-P-23

BJD_{UTC} (2,400,000 +)	Mag[a]	σ_{Mag}	Mag(orig)[b]	Filter
54632.73784	0.02143	0.00111	10.98360	*i*
54632.73870	0.01830	0.00116	10.98170	*i*
54632.73954	0.01503	0.00115	10.97810	*i*
54632.74039	0.01859	0.00115	10.98340	*i*
54632.74125	0.01123	0.00111	10.97530	*i*
54632.74208	0.02006	0.00109	10.98390	*i*
54632.74295	0.01831	0.00111	10.98220	*i*
54632.74381	0.01766	0.00114	10.97840	*i*
54632.74637	0.02025	0.00117	10.99540	*i*
54632.74722	0.01556	0.00112	10.97990	*i*

Notes. Same as those of Table 8.

(This table is available in its entirety in a machine-readable form in the online journal. A portion is shown here for guidance regarding its form and content.)

2. *HAT-P-21*—effective temperature $T_{\rm eff\star} = 5701 \pm 144$ K, stellar surface gravity $\log g_\star = 4.48 \pm 0.14$ (cgs), metallicity [Fe/H] $= +0.04 \pm 0.1$ dex, and projected rotational velocity $v \sin i = 4.1 \pm 0.5$ km s^{-1}.
3. *HAT-P-22*—effective temperature $T_{\rm eff\star} = 5338 \pm 88$ K, stellar surface gravity $\log g_\star = 4.52 \pm 0.14$ (cgs), metallicity [Fe/H] $= +0.26 \pm 0.08$ dex, and projected rotational velocity $v \sin i = 1.5 \pm 0.5$ km s^{-1}.
4. *HAT-P-23*—effective temperature $T_{\rm eff\star} = 5987 \pm 120$ K, stellar surface gravity $\log g_\star = 4.48 \pm 0.12$ (cgs), metallicity [Fe/H] $= +0.18 \pm 0.1$ dex, and projected rotational velocity $v \sin i = 8.0 \pm 0.5$ km s^{-1}.

The effective temperature and metallicity, along with the surface gravity taken as a luminosity indicator, can be used as constraints to infer the stellar mass and radius by comparison with stellar evolution models. However, the effect of $\log g_\star$ on the spectral line shapes is rather subtle, and as a result it is typically difficult to determine accurately, so that it is a rather poor luminosity indicator in practice. Unfortunately, a trigonometric parallax is not available for any of the host stars, since they were not included among the targets of the *Hipparcos* mission (Perryman et al. 1997). For planetary transits, another constraint is provided by the $a/R_\star$ normalized semi-major axis, which is closely related to $\rho_\star$, the mean stellar density. The quantity $a/R_\star$ can be derived directly from the combination of the transit light curves (Sozzetti et al. 2007) and the RV data (required for eccentric cases; see Section 3.3). This, in turn, allows us to improve on the determination of the spectroscopic parameters by supplying an indirect constraint on the weakly determined spectroscopic value of $\log g_\star$ that removes degeneracies. We take this approach here, as described below.

For each system, our initial values of $T_{\rm eff\star}$, $\log g_\star$, and [Fe/H] were used to determine auxiliary quantities needed in the global modeling of the follow-up photometry and RVs (specifically, the limb-darkening coefficients). This modeling, the details of which are described in Section 3.3, uses a Monte Carlo approach to deliver the numerical probability distribution of $a/R_\star$ and other fitted variables. When combining $a/R_\star$ (used as a proxy for luminosity) with assumed Gaussian distributions for $T_{\rm eff\star}$ and [Fe/H] based on the SME determinations, a comparison with stellar evolution models allows the probability distributions of other stellar properties to be inferred, including $\log g_\star$. Here we use the stellar evolution calculations from the Yonsei–Yale

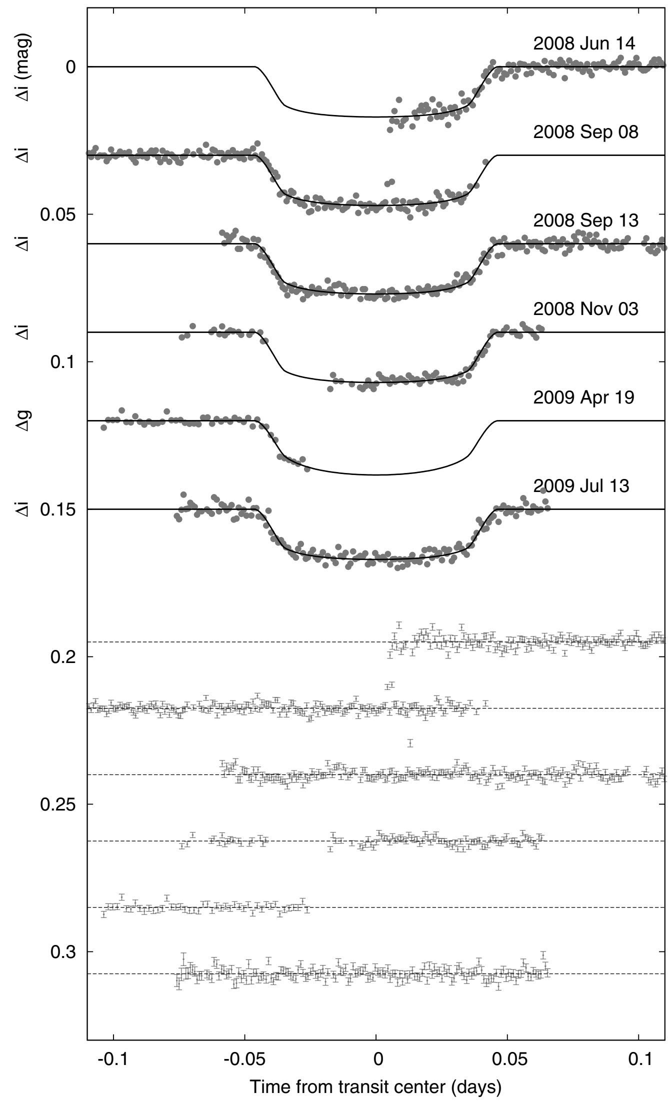

Figure 13. Similar to Figure 10; here we show the follow-up light curves for HAT-P-23.

group (YY; Yi et al. 2001) for all planets presented in this work. The comparison against the model isochrones was carried out for each of 10,000 Monte Carlo trial sets for HAT-P-21, HAT-P-22, and HAT-P-23, and for 20,000 Monte Carlo trial sets for HAT-P-20 (see Section 3.3). Parameter combinations corresponding to unphysical locations in the H-R diagram (26% of the trials for HAT-P-20, and less than 1% of the trials for the other objects) were ignored, and replaced with another randomly drawn parameter set. For each system we carried out a second SME iteration in which we adopted the value of $\log g_\star$ so determined and held it fixed in a new SME analysis (coupled with a new global modeling of the RV and light curves), adjusting only $T_{\rm eff\star}$, [Fe/H], and $v \sin i$. This gave the following:

1. *HAT-P-20*: $\log g_\star = 4.64 \pm 0.06$, $T_{\rm eff\star} = 4595 \pm 80$ K, [Fe/H] $= +0.35 \pm 0.08$, and $v \sin i = 2.1 \pm 0.5$ km s^{-1}.
2. *HAT-P-21*: $\log g_\star = 4.31 \pm 0.06$, $T_{\rm eff\star} = 5588 \pm 80$ K, [Fe/H] $= +0.01 \pm 0.08$, and $v \sin i = 3.5 \pm 0.5$ km s^{-1}.
3. *HAT-P-22*: $\log g_\star = 4.37 \pm 0.06$, $T_{\rm eff\star} = 5302 \pm 80$ K, [Fe/H] $= +0.24 \pm 0.08$, and $v \sin i = 0.5 \pm 0.5$ km s^{-1}.
4. *HAT-P-23*: $\log g_\star = 4.33 \pm 0.06$, $T_{\rm eff\star} = 5905 \pm 80$ K, [Fe/H] $= +0.15 \pm 0.04$, and $v \sin i = 8.1 \pm 0.5$ km s^{-1}.

Table 12
Stellar Parameters for HAT-P-20–HAT-P-23

Parameter	HAT-P-20	HAT-P-21	HAT-P-22	HAT-P-23	Source
Spectroscopic properties					
$T_{\rm eff\star}$ (K)...	4595 ± 80	5588 ± 80	5302 ± 80	5905 ± 80	SME[a]
[Fe/H]...	$+0.35 \pm 0.08$	$+0.01 \pm 0.08$	$+0.24 \pm 0.08$	$+0.15 \pm 0.04$	SME
$v \sin i$ (km s^{-1})...	2.1 ± 0.5	3.5 ± 0.5	0.5 ± 0.5	8.1 ± 0.5	SME
$v_{\rm mac}$ (km s^{-1})...	2.21	3.74	3.30	4.22	SME
$v_{\rm mic}$ (km s^{-1})...	0.85	0.85	0.85	0.85	SME
$\gamma_{\rm RV}$ (km s^{-1})...	-18.81 ± 0.68	-53.19 ± 0.09	$+12.49 \pm 0.28$	-15.10 ± 0.30	DS
Photometric properties					
V (mag)...	11.339	11.685	9.732	12.432	TASS[c]
$V - I_C$ (mag)...	1.50 ± 0.12	0.654 ± 0.097	0.992 ± 0.066	0.68 ± 0.12	TASS
J (mag)...	9.276 ± 0.022	10.503 ± 0.022	8.293 ± 0.023	11.103 ± 0.022	2MASS
H (mag)...	8.743 ± 0.021	10.154 ± 0.019	7.935 ± 0.029	10.846 ± 0.022	2MASS
K_s (mag)...	8.601 ± 0.019	10.111 ± 0.018	7.837 ± 0.021	10.791 ± 0.020	2MASS
$J - K$ (mag,ESO)...	0.715 ± 0.033	0.419 ± 0.031	0.486 ± 0.034	0.335 ± 0.032	2MASS
Derived properties					
$M_\star$ ($M_\odot$)...	0.756 ± 0.028	0.947 ± 0.042	0.916 ± 0.035	1.130 ± 0.035	YY+$a/R_\star$+SME[b]
$R_\star$ ($R_\odot$)...	0.694 ± 0.021	1.105 ± 0.083	1.040 ± 0.044	1.203 ± 0.074	YY+$a/R_\star$+SME
$\log g_\star$ (cgs)...	4.63 ± 0.02	4.33 ± 0.06	4.36 ± 0.04	4.33 ± 0.05	YY+$a/R_\star$+SME
$L_\star$ ($L_\odot$)...	0.19 ± 0.02	$1.06^{+0.20}_{-0.16}$	0.77 ± 0.09	1.58 ± 0.23	YY+$a/R_\star$+SME
M_V (mag)...	7.07 ± 0.17	4.80 ± 0.19	5.22 ± 0.14	4.31 ± 0.16	YY+$a/R_\star$+SME
M_K (mag,ESO)...	4.42 ± 0.09	3.12 ± 0.16	3.30 ± 0.10	2.86 ± 0.14	YY+$a/R_\star$+SME
$J - K$ (mag,ESO)...	0.66 ± 0.02	0.44 ± 0.02	0.50 ± 0.02	0.37 ± 0.01	YY+$a/R_\star$+SME
Age (Gyr)...	$6.7^{+5.7}_{-3.8}$	10.2 ± 2.5	12.4 ± 2.6	4.0 ± 1.0	YY+$a/R_\star$+SME
Distance (pc)...	70 ± 3	254 ± 19	82 ± 3	393 ± 25	YY+$a/R_\star$+SME

Notes.
[a] SME = "Spectroscopy Made Easy" package for the analysis of high-resolution spectra (Valenti & Piskunov 1996). These parameters rely primarily on SME, but have a small dependence also on the iterative analysis incorporating the isochrone search and global modeling of the data, as described in the text.
[b] YY+$a/R_\star$+SME = Based on the YY isochrones (Yi et al. 2001), $a/R_\star$ as a luminosity indicator, and the SME results.
[c] From Droege et al. (2006).

In each case the conservative uncertainties for $T_{\rm eff\star}$ and [Fe/H] have been increased by a factor of two over their formal values, as before. For each system, a further iteration did not change $\log g_\star$ significantly, so we adopted the values stated above as the final atmospheric properties of the stars. They are collected in Table 12.

With the adopted spectroscopic parameters the model isochrones yield the stellar mass and radius, and other properties. These are listed for each of the systems in Table 12. According to these models HAT-P-20 is a dwarf star with an estimated age of $6.7^{+5.7}_{-3.8}$ Gyr, HAT-P-21 is a slightly evolved star with an estimated age of 10.2 ± 2.5 Gyr, HAT-P-22 is a slightly evolved star with an estimated age of 12.4 ± 2.6 Gyr, and HAT-P-23 is a slightly evolved star with an estimated age of 4.0 ± 1.0 Gyr. The inferred location of each star in a diagram of $a/R_\star$ versus $T_{\rm eff\star}$, analogous to the classical H-R diagram, is shown in Figure 14. In all cases the stellar properties and their 1σ and 2σ confidence ellipsoides are displayed against the backdrop of model isochrones for a range of ages, and the appropriate stellar metallicity. For comparison, the locations implied by the initial SME results are also shown (in each case with a triangle).

The stellar evolution modeling provides color indices (see Table 12) that may be compared against the measured values as a sanity check. For each star, the best available measurements are the near-infrared magnitudes from the 2MASS Catalog (Skrutskie et al. 2006), which are given in Table 12. These are converted to the photometric system of the models (ESO system) using the transformations by Carpenter (2001). The resulting color indices are also shown in Table 12 for HAT-P-20 through HAT-P-23, respectively. Indeed, the colors from the stellar evolution models and from the observations agree for all of the host stars within 2σ. The distance to each object was computed from the absolute K magnitude from the models and the 2MASS K_s magnitudes, which has the advantage of being less affected by extinction than optical magnitudes. The results are given in Table 12, where in all cases the uncertainty excludes possible systematics in the model isochrones that are difficult to quantify.

3.2. Excluding Blend Scenarios

Our initial spectroscopic analyses discussed in Sections 2.2 and 2.3 rule out the most obvious astrophysical false positive scenarios. However, more subtle phenomena such as blends (contamination by an unresolved eclipsing binary, whether in the background or associated with the target) can still mimic both the photometric and spectroscopic signatures we see. In the following section, we investigate whether such scenarios may have caused the observed photometric and spectroscopic features.

3.2.1. Spectral Line-bisector Analysis

Following Torres et al. (2007), we explored the possibility that the measured RVs are not real, but are instead caused by distortions in the spectral line profiles due to contamination from a nearby unresolved eclipsing binary. A bisector span (BS) analysis for each system based on the Keck spectra was done as described in Section 5 of Bakos et al. (2007). In general, none of the Keck/HIRES spectra suffer significant sky contamination. Nevertheless, we calculated the sky contamination factors (SCF) as described in Hartman et al. (2009), and corrected for the minor correlation between SCF and BS. The results are exhibited

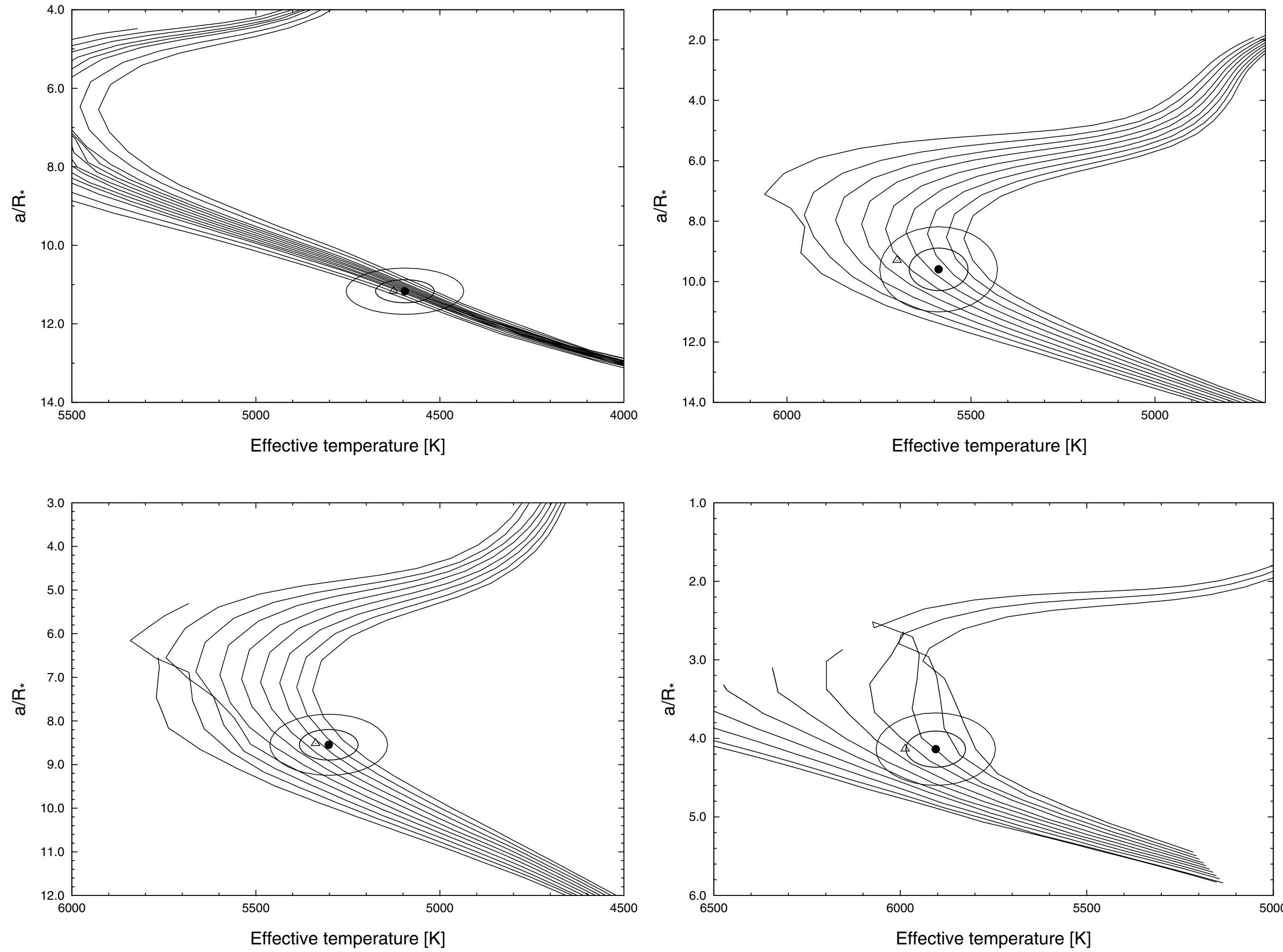

Figure 14. Upper left: model isochrones from Yi et al. (2001) for the measured metallicity of HAT-P-20, [Fe/H] = +0.35, and ages of 3.0, 4.0, 5.0, 5.5, 6.0, 6.5, 7.0, 7.5, 8.0, 8.5, 9.0, 10.0, and 11.0 Gyr (left to right). The adopted values of $T_{\rm eff\star}$ and $a/R_\star$ are shown together with their 1σ and 2σ confidence ellipsoids. The initial values of $T_{\rm eff\star}$ and $a/R_\star$ from the first SME and light curve analyses are represented with a triangle. Upper right: same as upper left, here we show the results for HAT-P-21, with [Fe/H] = +0.01, and ages of 5.0, 6.0, 7.0, 8.0, 9.0, 10.0, 11.0, 12.0, and 13.0 Gyr (left to right). Lower left: same as upper left, here we show the results for HAT-P-22, with [Fe/H] = +0.24, and ages of 5.0, 6.0, 7.0, 8.0, 9.0, 10.0, 11.0, 12.0, 13.0, and 14.0 Gyr (left to right). Lower right: same as upper left, here we show the results for HAT-P-23, with [Fe/H] = +0.15, and ages of 0.2, 0.5, 1.0, 1.5, 2.0, 2.5, 3.0, 3.5, 4.0, 4.5, and 5.0 Gyr (left to right).

Table 13
Summary of RV versus BS Correlations

Name	R_{s1}[a]	FAP_1[b]	R_{s2}[c]	FAP_2[d]
HAT-P-20	−0.73	2.46%	−0.92	0.05%
HAT-P-21	−0.24	39%	−0.20	47%
HAT-P-22	0.33	30%	0.27	37%
HAT-P-23	0.27	37%	0.27	37%

Notes.
[a] The Spearman correlation coefficient between the bisector (BS) variations and the radial velocities (RV).
[b] False alarm probability for R_{s1}.
[c] The Spearman correlation coefficient between BS corrected for the sky contamination factor (SCF) and the RVs.
[d] False alarm probability for R_{s2}.

in Figure 15, where we show the SCF–BS and RV–$\mathrm{BS_{SCF}}$ (BS after SCF correction) plots for each planetary system. We also calculated the Spearman rank-order correlation coefficients (denoted as R_s for the RV versus BS quantities and the false alarm probabilities (see Table 13). There is no correlation for HAT-P-21, HAT-P-22, and HAT-P-23, and thus the interpretation of these systems as transiting planets is clear. There is an anti-correlation present for HAT-P-20, which is strengthened when the SCF correction is applied. A plausible explanation for this is that the neighboring star at 6″ separation (see Figure 5) is bleeding into the slit, even though we were careful during the observations to keep the slit centered on the main target, and adjusted the slit orientation to be perpendicular to the direction to the neighbor. We simulated this scenario, and calculated the expected BS as a function of RV due to the neighbor, assuming that the two stars have the same systemic velocity and the seeing is 1″. Indeed, we get a slight anti-correlation from this simulation, and the range of magnitude in the BS variation is consistent with the observations. It is also possible that some of the anti-correlation is due to the fact that the slit was not in vertical angle for many of the observations. The non-vertical slit mode may result in wavelength-dependent slit losses due to atmospheric dispersion, and this could bring in a correlation with the sky background, and change the shape of the spectral lines.

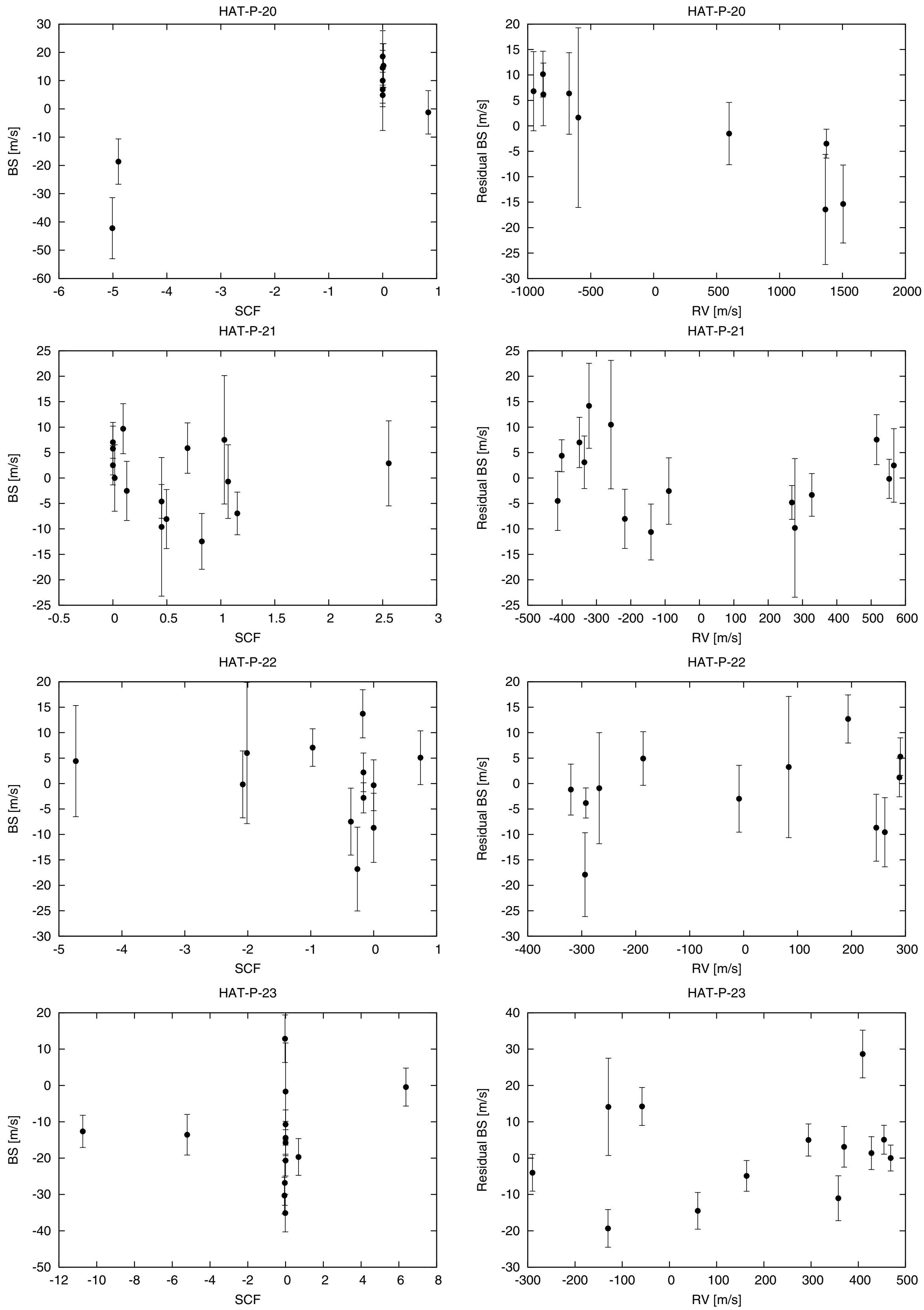

Figure 15. Panels on the left show the bisector spans (BS) as a function of sky contamination factor (SCF). Panels on the right exhibit the SCF-corrected BS as a function of the RVs. The individual planets are labeled.

3.3. Global Modeling of the Data

This section describes the procedure we followed for each system to model the HATNet photometry, the follow-up photometry, and the RVs simultaneously. Our model for the follow-up light curves used analytic formulae based on Mandel & Agol (2002) for the eclipse of a star by a planet, with limb darkening being prescribed by a quadratic law. The limb-darkening coefficients for the Sloan g-band, Sloan i-band, and Sloan z-band were interpolated from the tables by Claret (2004) for the spectroscopic parameters of each star as determined from the SME analysis (Section 3.1). The transit shape was parameterized by the normalized planetary radius $p \equiv R_p/R_\star$, the square of the impact parameter b^2, and the reciprocal of the half-duration of the transit $\zeta/R_\star$. We chose these parameters because of their simple geometric meanings and the fact that these show negligible correlations (see Bakos et al. 2010). The relation between $\zeta/R_\star$ and the quantity $a/R_\star$, used in Section 3.1, is given by

$$a/R_\star = P/2\pi(\zeta/R_\star)\sqrt{1-b^2}\sqrt{1-e^2}/(1+e\sin\omega) \quad (1)$$

(see, e.g., Tingley & Sackett 2005; Kipping 2010). Note the subtle dependency of $a/R_\star$ on the $k \equiv e\cos\omega$ and $h \equiv e\sin\omega$ Lagrangian orbital parameters that are typically derived from the RV data (ω is the longitude of periastron). This dependency is often ignored in the literature, and $a/R_\star$ is quoted as a "pure" light curve parameter. Of course, if high-quality secondary eclipse observations are available that determine both the location and duration of the occultation, then k and h can be determined without RV data. Our model for the HATNet data was the simplified "P1P3" version of the Mandel & Agol (2002) analytic functions (an expansion in terms of Legendre polynomials), for the reasons described in Bakos et al. (2010). Following the formalism presented by Pál (2009a), the RVs were fitted with an eccentric Keplerian model parameterized by the semi-amplitude K and Lagrangian elements k and h. Note that we allowed for an eccentric orbit for all planets, even if the results were consistent with a circular orbit. There are several reasons for this: (1) many of the close-in hot Jupiters show eccentric orbits, thus the assumption of fixing $e = 0$ has no physical justification (while this has been customary in early discoveries relying on very few data points), (2) the error bars on various other derived quantities (including $a/R_\star$) are more realistic with the inclusion of eccentricity, and (3) non-zero eccentricities can be very important in proper interpretation of these systems.

We assumed that there is a strict periodicity in the individual transit times. For each system we assigned the transit number $N_{\rm tr} = 0$ to a complete follow-up light curve. For HAT-P-20b this was the light curve gathered on 2009 October 21, for HAT-P-21b: 2010 February 19, HAT-P-22b: 2009 February 28, and HAT-P-23b: 2008 September 13. The adjustable parameters in the fit that determine the ephemeris were chosen to be the time of the first transit center observed with HATNet ($T_{c,-252}$, $T_{c,-286}$, $T_{c,-135}$, and $T_{c,-312}$ for HAT-P-20b through HAT-P-23b, respectively) and that of the last transit center observed with the FLWO 1.2 m telescope ($T_{c,0}$, $T_{c,1}$, $T_{c,19}$, and $T_{c,250}$ for HAT-P-20b through HAT-P-23b, respectively). We used these as opposed to period and reference epoch in order to minimize correlations between parameters (see Pál et al. 2008). Times of mid-transit for intermediate events were interpolated using these two epochs and the corresponding transit number of each event, $N_{\rm tr}$. The eight main parameters describing the physical model for each system were thus the first and last transit center times, $R_p/R_\star$, b^2, $\zeta/R_\star$, K, $k \equiv e\cos\omega$, and $h \equiv e\sin\omega$. For HAT-P-20b, HAT-P-22b, and HAT-P-23b, three additional parameters were included (for each system) that have to do with the instrumental configuration (dilution factor, out-of-transit magnitudes, gamma velocities; see later). For HAT-P-21b seven additional parameters were included, because it was observed in three different HATNet fields. These are the HATNet dilution factor $B_{\rm inst}$ (one for each HATNet field), which accounts for dilution of the transit in the HATNet light curve from background stars due to the broad point spread function (PSF; 25″ FWHM) and for reduction of the HATNet transit depth due to the TFA procedure, the HATNet out-of-transit magnitude $M_{0,\rm HATNet}$ (one for each HATNet field), and the relative zero-point $\gamma_{\rm rel}$ of the Keck RVs.

The physical model was extended with an instrumental model that describes brightness variations caused by systematic errors in the measurements. This was done in a similar fashion to the analysis presented by Bakos et al. (2010), i.e., using the "ELTG" (EPD local, TFA global) method for correcting the follow-up light curves. In all cases the total number of fitted parameters (43, 36, 33, and 67 for HAT-P-20b through HAT-P-23b) was much smaller than the number of data points (755, 1172, 892, and 953, counting only RV measurements and follow-up photometry measurements). The joint fit was performed as described in Bakos et al. (2010) using a Markov Chain Monte Carlo approach (MCMC; see Ford 2006).

The a priori distributions of the parameters for these chains were chosen to be Gaussian, with eigenvalues and eigenvectors derived from the Fisher covariance matrix for the best-fit solution. The MCMC analysis provided the full a posteriori probability distributions of all adjusted variables.

Following this procedure we obtained the a posteriori distributions for all other quantities of interest such as $a/R_\star$. As described in Section 3.1, $a/R_\star$ was used together with stellar evolution models to infer a value for $\log g_\star$ that is significantly more accurate than the spectroscopic value. The improved estimate was in turn applied to a second iteration of the SME analysis, as explained previously, in order to obtain better estimates of $T_{\rm eff\star}$ and [Fe/H]. The global modeling was then repeated with updated limb-darkening coefficients based on those new spectroscopic determinations. The resulting geometric parameters pertaining to the light curves and velocity curves for each system are listed in Table 14.

Included in each table is the RV "jitter," which is a noise term that we added in quadrature to the internal errors for the RVs in order to achieve $\chi^2/{\rm dof} = 1$ from the RV data for the global fit. The jitter is a combination of assumed astrophysical noise intrinsic to the star, plus instrumental noise rising from uncorrected instrumental effects (such as a template spectrum taken under suboptimal conditions).

The planetary parameters and their uncertainties were derived by combining the a posteriori distributions for the stellar, light curve, and RV parameters. In this way we find masses and radii for each planet. These and other planetary parameters are listed at the bottom of Table 14, and further discussed in Section 4.

4. DISCUSSION

4.1. HAT-P-20b

HAT-P-20b is a very massive ($M_p = 7.246 \pm 0.187\,M_{\rm J} = 2302.9 \pm 59.5\,M_\oplus$) and very compact ($R_p = 0.867 \pm 0.033\,R_{\rm J}$) hot Jupiter orbiting a K3 (Skiff 2009) star. With $\rho_p = 13.78 \pm 1.50$ g cm^{-3}, HAT-P-20b is among the most massive and most dense transiting planets known (see Figure 16).

Table 14
Orbital and Planetary Parameters for HAT-P-20b–HAT-P-23b

Parameter	HAT-P-20b	HAT-P-21b	HAT-P-22b	HAT-P-23b
Light curve parameters				
P (days) . . .	2.875317 ± 0.000004	4.124481 ± 0.000007	3.212220 ± 0.000009	1.212884 ± 0.000002
T_c (BJD$_{\rm UTC}$)[a] . . .	$2455080.92661 \pm 0.00021$	$2454996.41312 \pm 0.00069$	$2454930.22001 \pm 0.00025$	$2454852.26464 \pm 0.00018$
T_{14} (days)[a] . . .	0.0770 ± 0.0008	0.1530 ± 0.0027	0.1196 ± 0.0014	0.0908 ± 0.0007
$T_{12} = T_{34}$ (days)[a] . . .	0.0137 ± 0.0009	0.0184 ± 0.0029	0.0144 ± 0.0013	0.0105 ± 0.0007
$a/R_\star$ . . .	11.17 ± 0.29	9.60 ± 0.71	8.55 ± 0.35	4.14 ± 0.23
$\zeta/R_\star$ . . .	31.32 ± 0.22	14.81 ± 0.15	18.97 ± 0.09	24.90 ± 0.12
$R_p/R_\star$ . . .	0.1284 ± 0.0016	0.0950 ± 0.0022	0.1065 ± 0.0017	0.1169 ± 0.0012
b^2 . . .	$0.398^{+0.032}_{-0.034}$	$0.298^{+0.089}_{-0.118}$	$0.217^{+0.052}_{-0.065}$	$0.105^{+0.053}_{-0.049}$
$b \equiv a \cos i/R_\star$ . . .	$0.631^{+0.025}_{-0.028}$	$0.546^{+0.074}_{-0.139}$	$0.466^{+0.052}_{-0.083}$	$0.324^{+0.070}_{-0.101}$
i (deg) . . .	86.8 ± 0.2	87.2 ± 0.7	$86.9^{+0.6}_{-0.5}$	85.1 ± 1.5
Limb-darkening coefficients[b]				
a_i (linear term) . . .	0.4719	0.2976	0.3587	0.2524
b_i (quadratic term) . . .	0.2174	0.3131	0.2831	0.3426
a_g . . .	. . .	. . .	0.7080	0.5311
b_g . . .	. . .	. . .	0.1165	0.2539
RV parameters				
K (m s^{-1}) . . .	1246.0 ± 8.1	548.3 ± 14.2	313.3 ± 4.2	368.5 ± 17.6
$k_{\rm RV}$[c] . . .	0.012 ± 0.004	0.147 ± 0.011	-0.008 ± 0.008	-0.048 ± 0.023
$h_{\rm RV}$[c] . . .	-0.007 ± 0.008	-0.175 ± 0.019	0.004 ± 0.016	0.090 ± 0.052
e . . .	0.015 ± 0.005	0.228 ± 0.016	0.016 ± 0.009	0.106 ± 0.044
ω (deg) . . .	317 ± 130	309 ± 3	156 ± 66	118 ± 25
RV jitter (m s^{-1}) . . .	15.7	26.4	9.9	34.7
Secondary eclipse parameters (derived)				
T_s (BJD$_{\rm UTC}$) . . .	2455082.385 ± 0.007	2454998.865 ± 0.029	2454931.809 ± 0.016	2454852.834 ± 0.018
$T_{s,14}$ . . .	0.0764 ± 0.0010	0.1163 ± 0.0068	0.1204 ± 0.0032	0.1064 ± 0.0095
$T_{s,12}$ . . .	0.0134 ± 0.0009	0.0117 ± 0.0015	0.0145 ± 0.0014	0.0129 ± 0.0020
Planetary parameters				
M_p ($M_{\rm J}$) . . .	7.246 ± 0.187	4.063 ± 0.161	2.147 ± 0.061	2.090 ± 0.111
R_p ($R_{\rm J}$) . . .	0.867 ± 0.033	1.024 ± 0.092	1.080 ± 0.058	1.368 ± 0.090
$C(M_p, R_p)$[d] . . .	0.50	0.28	0.36	0.56
ρ_p (g cm^{-3}) . . .	13.78 ± 1.50	$4.68^{+1.59}_{-0.99}$	$2.11^{+0.40}_{-0.29}$	1.01 ± 0.18
$\log g_p$ (cgs) . . .	4.38 ± 0.03	3.98 ± 0.08	3.66 ± 0.05	3.44 ± 0.05
a (AU) . . .	0.0361 ± 0.0005	0.0494 ± 0.0007	0.0414 ± 0.0005	0.0232 ± 0.0002
$T_{\rm eq}$ (K) . . .	970 ± 23	1283 ± 50	1283 ± 32	2056 ± 66
Θ[e] . . .	0.794 ± 0.031	0.413 ± 0.038	0.179 ± 0.010	0.062 ± 0.004
$F_{\rm per}$ (10^8 erg s^{-1} cm^{-2})[f] . . .	2.06 ± 0.20	10.0 ± 1.5	6.33 ± 0.67	50.0 ± 11.4
F_{ap} (10^8 erg s^{-1} cm^{-2})[f] . . .	1.94 ± 0.19	3.96 ± 0.66	5.91 ± 0.60	32.7 ± 2.7
$\langle F \rangle$ (10^8 erg s^{-1} cm^{-2})[f] . . .	2.00 ± 0.19	6.12 ± 0.97	6.12 ± 0.62	40.3 ± 5.3

Notes.
[a] T_c: reference epoch of mid-transit that minimizes the correlation with the orbital period. It corresponds to $N_{\rm tr} = -16$. BJD is calculated from UTC. T_{14}: total transit duration, time between first to last contact; $T_{12} = T_{34}$: ingress/egress time, time between first and second, or third and fourth contact.
[b] Values for a quadratic law, adopted from the tabulations by Claret (2004) according to the spectroscopic (SME) parameters listed in Table 12.
[c] $k = e\cos\omega$ and $h = e\sin\omega$. These orbital parameters are derived from the global modeling, and are primarily determined by the RV data.
[d] Correlation coefficient between the planetary mass M_p and radius R_p.
[e] The Safronov number is given by $\Theta = \frac{1}{2}(V_{\rm esc}/V_{\rm orb})^2 = (a/R_p)(M_p/M_\star)$ (see Hansen & Barman 2007).
[f] Incoming flux per unit surface area. $\langle F \rangle$ is averaged over the orbit.

Modeling HAT-P-20b may be a challenge, as the oldest (4 Gyr, i.e., yielding the most compact planets) Fortney et al. (2007) models with $M_p = 2154\,M_\oplus$ total mass and $100\,M_\oplus$ core mass predict a much bigger radius ($1.04\,R_{\rm J}$). The observed radius of $0.87\,M_{\rm J}$ would require a very high metal content. We note that the host star is one of the most metal-rich stars that have a transiting planet ([Fe/H] $= +0.35 \pm 0.08$). Curiously, HAT-P-20b orbits a fairly late-type star (K3), as compared to most of the massive hot Jupiters that orbit ∼F5 dwarfs. The irradiation HAT-P-20b receives is one of the smallest, clearly making it a pL class exoplanet (Fortney et al. 2008): $\langle F \rangle = (2.00 \pm 0.19) \times 10^8$ erg s^{-1} cm^{-2}, comparable to the mean flux per orbit for another "heavy" planet HD 17156b on a 21 day period orbit. HAT-P-20 is an outlier in the M_p–$M_\star$ plane; it is a relatively small mass star harboring a very massive planet. Another outlier (albeit to a much lesser extent) with similar planetary radius and stellar mass is WASP-10b (Johnson et al. 2009; Christian et al. 2009), but this planet has less than half of the mass of HAT-P-20b ($3.09\,M_{\rm J}$). We also calculated the maximum mass of a stable moon for both the prograde and retrograde cases, and derived $0.128\,M_\oplus$ and $8.31\,M_\oplus$, respectively, i.e., HAT-P-20b can harbor a fairly massive moon. An $8.31\,M_\oplus$ retrograde moon would cause ∼10 s variations in the transit times, which is marginally detectable from the ground.

HAT-P-20 has a close-by faint and red companion star at ∼6″.86 separation. Based on the Palomar sky survey archival

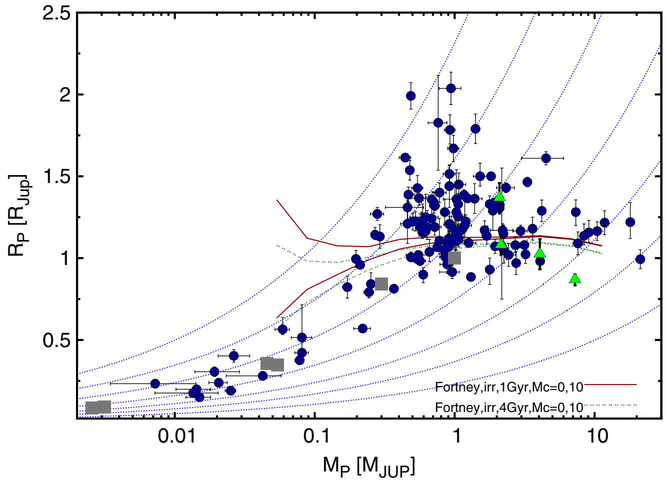

Figure 16. Mass–radius diagram of known TEPs (filled circles). HAT-P-20b–HAT-P-23b are shown as filled triangles. Overlaid are Fortney et al. (2007) planetary isochrones interpolated to the solar equivalent semi-major axis of HAT-P-20b for ages of 1.0 Gyr (upper, solid lines) and 4 Gyr (lower, dash-dotted lines) and core masses of 0 and 10 $M_\oplus$ (upper and lower lines, respectively), as well as isodensity lines for 0.1, 0.3, 0.9, 3.0, 9.0, 25.0, and 100.0 g cm^{-3} (dotted lines from top to bottom). Solar system planets are shown with filled squares.

(A color version of this figure is available in the online journal.)

plates, we confirm that they form a close common proper motion pair, thus it is very likely that the two stars are physically associated. The binary has appeared in the Washington Double Star compilation (WDS) as POU2795, and was discovered by Pourteau (1933). Furthermore, based on the summary of observations in the WDS, there is already a hint of orbital motion of the companion to HAT-P-20 over the last century. The position angle of the companion changed from P.A. = 323° to P.A. = 320° over the course of 89 years (between 1909 and 1998), and it seems to be retrograde on the sky (clockwise). Thus, HAT-P-20 is yet another example of a massive planet in a binary system (Udry et al. 2002). The binary companion makes this system ideal for high precision ground or space-based studies, as it provides a natural comparison source, even though it has a later spectral type.

4.2. HAT-P-21b

HAT-P-21b has a mass of $M_p = 4.063 \pm 0.161\, M_J$, radius of $R_p = 1.024 \pm 0.092\, R_J$, mean density of $\rho_p = 4.68^{+1.59}_{-0.99}$ g cm^{-3}, and orbits on a moderately eccentric orbit with $e = 0.228 \pm 0.016$, $\omega = 309° \pm 3°$. The transits occur near apastron. As noted by Buchhave et al. (2010), 4 M_J mass planets are quite rare in the sample of currently known transiting exoplanets, and the only siblings of HAT-P-21b are WASP-32b (3.6 M_J; Maxted et al. 2010), HD 80606b (4.08 M_J; Naef et al. 2001), and HAT-P-16b (4.19 M_J; Buchhave et al. 2010). WASP-32b and HAT-P-16b are similar to each other with $P \sim 2.7$–2.8 day orbital periods and large radii ($R_p > 1.15\, R_J$ in both cases), but dissimilar from the longer period, smaller radius, and more eccentric planet HAT-P-21b. HD 80606b, on the other hand, has a similar radius than HAT-P-21b, and orbits on an extremely eccentric ($e = 0.93$) orbit with a period of 111 days. It appears that HAT-P-21b is thus an unusual, short-period, eccentric, massive, and compact planet.

The only models from Fortney et al. (2007) consistent with the observed radius are 4 Gyr models with 100 $M_\oplus$ core mass, yielding 1.05 R_J radius. HAT-P-21b has a very high mean density; similar to HD 80606b and WASP-14b.

The flux received by the planet varies between $(10.0 \pm 1.5) \times 10^8$ erg s^{-1} cm^{-2} and $(3.96 \pm 0.66) \times 10^8$ erg s^{-1} cm^{-2}. Interestingly, this puts HAT-P-21b on the bordlerline between pL (low irradiation) and pM (high irradiation) planets. At the time of occultation, HAT-P-21b is just approaching its periastron, thus entering the irradiation level quoted for pM-type planets.

4.3. HAT-P-22b

HAT-P-22b has a mass of $M_p = 2.147 \pm 0.061\, M_J$, radius of $R_p = 1.080 \pm 0.058\, R_J$, and mean density of $\rho_p = 2.11^{+0.40}_{-0.29}$ g cm^{-3}. HAT-P-22b orbits a fairly metal-rich ([Fe/H] = + 0.24 ± 0.08), bright ($V = 9.732$), and close-by (82 ± 3 pc) star. Similar to HAT-P-20, the host star has a faint and red neighbor at 9″ separation that is co-moving with HAT-P-22 (based on the POSS plates and recent Keck/HIRES snapshots), thus they are likely to form a physical pair.

HAT-P-22b belongs to the moderately massive ($\sim 2\, M_J$) and compact ($R_p \approx 1\, R_J$) hot Jupiters, such as HAT-P-15b ($M_p = 1.95 M_J$, $R_p = 1.07\, R_J$; Kovács et al. 2010), HAT-P-14b ($M_p = 2.23 M_J$, $R_p = 1.15\, R_J$; Torres et al. 2010), and WASP-8b ($M_p = 2.25 M_J$, $R_p = 1.05\, R_J$; Queloz et al. 2010).

HAT-P-22b is broadly consistent with the models of Fortney et al. (2008). For 300 Myr, 1 Gyr, and 4 Gyr models, it requires a 100 $M_\oplus$, 50 $M_\oplus$, and 25 $M_\oplus$ core, respectively, to have a radius of $\sim 1.08\, R_J$. The low incoming flux (see Table 14) means that HAT-P-22b is a pL class planet. HAT-P-22b can harbor a 0.96 $M_\oplus$ mass retrograde moon, which would cause transit timing variations (TTVs) of ∼2 s.

4.4. HAT-P-23b

HAT-P-23b has a mass of $M_p = 2.090 \pm 0.111\, M_J$, radius of $R_p = 1.368 \pm 0.090\, R_J$, and mean density of $\rho_p = 1.01 \pm 0.18$ g cm^{-3}. It belongs to the inflated group of 2 M_J planets. A few other planets which are similar to it include TrES-3b ($M_p = 1.91 M_J$, $R_p = 1.37\, R_J$; Sozzetti et al. 2009), Kepler-5b ($M_p = 2.10 M_J$, $R_p = 1.31\, R_J$; Kipping & Bakos 2011; Koch et al. 2010), WASP-46b ($M_p = 2.10 M_J$, $R_p = 1.33\, R_J$; Anderson et al. 2011), and CoRoT-11b ($M_p = 2.33 M_J$, $R_p = 1.43\, R_J$; Gandolfi et al. 2010). The orbit is nearly circular, with the eccentricity being marginally significant. The reason for the somewhat higher than usual errors in the RV parameters is the high jitter of the star (34.7 m s^{-1}), which may be related to the moderately high $v \sin i = 8.1 \pm 0.5$ km s^{-1} and the very close-in orbit of HAT-P-23b. The Fortney et al. (2008) models cannot reproduce the observed radius of HAT-P-23b; even for the youngest, (300 Myr) coreless models, the theoretical radius for its mass is 1.25 R_J. HAT-P-23b orbits its host star on a very close-in orbit. The orbital period is only 1.2129 days; almost identical to that of OGLE-TR-56b (1.21192 days). The nominal planetary radius of the two objects is also the same within 1%, but OGLE-TR-56b is much less massive (1.39 M_J). The flux falling on HAT-P-23b from its host star is one of the highest (i.e., belongs to the pM class objects), and is similar to that of HAT-P-7b and OGLE-TR-56b. We also calculated the spiral infall timescale for each new discovery based on Levrard et al. (2009) and Dobbs-Dixon et al. (2004). By assuming that the stellar dissipation factor is $Q_\star = 10^6$, the infall time for HAT-P-23b is $\tau_{\rm infall} = 7.5^{+2.9}_{-1.8}$ Myr, one of the shortest among exoplanets.

The Rossiter–McLaughlin (R-M) effect for HAT-P-23b should be quite significant, given the moderately high

$v \sin i = 8.1 \pm 0.5\,\mathrm{km\,s^{-1}}$ of the host star and the $\Delta i =$ 17 mmag deep transit. The impact parameter is also "ideal" ($b = 0.324^{+0.070}_{-0.101}$), i.e., it is not equatorial ($b = 0$), where there would be a strong degeneracy between the stellar rotational velocity $v \sin i$ and the sky-projected angle of the stellar spin axis and the orbital normal, λ, and is also far from grazing, where the transit is short, and other system parameters have lower accuracy. The effective temperature of the star ($T_{\mathrm{eff}\star} = 5905 \pm 80\,\mathrm{K}$) is close to the critical temperature of 6250 K noted recently by Winn et al. (2010), which may be a borderline between systems where the stellar spin axes and planetary orbital normals are preferentially aligned ($T_{\mathrm{eff}\star} < 6250\,\mathrm{K}$) and those that are misaligned ($T_{\mathrm{eff}\star} > 6250\,\mathrm{K}$). An alternative hypothesis has been brought up by Schlaufman (2010), where misaligned stellar spin axes and orbital normals are related to the mass of the host star. The mass of HAT-P-23 (1.13 ± 0.04) is sufficiently close to the suggested dividing line of $M_\star = 1.2\,M_\odot$, and thus it will provide an excellent additional test for these ideas.[17]

4.5. Summary

We presented the discovery of four new massive transiting planets, and provided accurate characterization of the host star and planetary parameters. These four new systems are very diverse, and significantly expand the sample of massive ($M_p \gtrsim 2\,M_{\mathrm{J}}$) planets. Two of the new discoveries orbit stars that have fainter companions, which are probably physically associated. The new discoveries do not tend to enhance the mass–eccentricity correlation, since only one (HAT-P-21b) is significantly eccentric. Also, the tentative mass–$v \sin i$ correlation noted in Section 1 is weakened by the new discoveries. The heavier mass planets (HAT-P-20b and HAT-P-21b) are inconsistent with current theoretical models in that they are extremely dense, and would require a substantial core (or high metal content) to have such small radii. One planet (HAT-P-23b) is also inconsistent with the models (unless we assume that the planet is very young), but in the sense that it has a density that is lower than can be explained by the models. It has been noted by Winn et al. (2010) and Schlaufman (2010) that systems exhibiting stellar spin axis–planetary orbital normal misalignment are preferentially eccentric and heavy mass planets (in addition to the dependence noted by these authors of the spin–orbit angle on the effective temperature or mass of the host star). The four new planets presented in this work will provide additional important tests for checking these conjectures. The host stars are all bright ($9.7 < V < 12.4$), and thus enable in-depth future characterization of these systems.

HATNet operations have been funded by NASA grants NNG04GN74G, NNX08AF23G, and SAO IR&D grants. Work of G.Á.B. was supported by the Postdoctoral Fellowship of the NSF Astronomy and Astrophysics Program (AST-0702843 and AST-0702821, respectively). G.T. acknowledges partial support from NASA grant NNX09AF59G. We acknowledge partial support also from the *Kepler* Mission under NASA Cooperative Agreement NCC2-1390 (D.W.L., PI). G.K. thanks the Hungarian Scientific Research Foundation (OTKA) for support through grant K-81373. This research has made use of Keck telescope time granted through NOAO and NASA, and uses observations obtained with facilities of the Las Cumbres Observatory Global Telescope. The authors recognize and acknowledge the very significant cultural role and reverence that the summit of Mauna Kea has always had within the indigenous Hawaiian community. We are most fortunate to have the opportunity to conduct observations from this mountain.

[17] Following the submission of this paper, Moutou et al. (2011) reported a detection of the R-M effect for HAT-P-23b. They find an amplitude of $\sim$50 m s^{-1} for this effect, and measure a projected spin–orbit angle of $+15^\circ \pm 22^\circ$ for this system.

REFERENCES

Alard, C. 2000, A&AS, 144, 363
Alonso, R., Brown, T. M., Torres, G., et al. 2004, ApJ, 613, L153
Anderson, D. R., Collier Cameron, A., Gillon, M., et al. 2011, arXiv:1105.3179
Baglin, A., Auvergne, M., Boisnard, L., et al. 2006, 36th COSPAR Scientific Assembly, Meeting Abstract, 3749
Bakos, G. Á., Kovács, G., Torres, G., et al. 2007, ApJ, 670, 826
Bakos, G. Á., Noyes, R. W., Kovács, G., et al. 2004, PASP, 116, 266
Bakos, G. Á., Torres, G., Pál, A., et al. 2010, ApJ, 710, 1724
Baraffe, I., Chabrier, G., & Barman, T. 2008, A&A, 482, 315
Baraffe, I., Chabrier, G., & Barman, T. 2010, Rep. Prog. Phys., 73, 016901
Borucki, W. J., Koch, D., Basri, G., et al. 2010, Science, 327, 977
Bramich, D. M. 2008, MNRAS, 386, L77
Buchhave, L. A., Bakos, G. A., Hartman, J. D., et al. 2010, ApJ, 720, 1118
Butler, R. P., Marcy, G. W., Williams, E., et al. 1996, PASP, 108, 500
Carpenter, J. M. 2001, AJ, 121, 2851
Chatterjee, S., Ford, E. B., Matsumura, S., & Rasio, F. A. 2008, ApJ, 686, 580
Christian, D. J., Gibson, N. P., Simpson, E. K., et al. 2009, MNRAS, 392, 1585
Claret, A. 2004, A&A, 428, 1001
Deleuil, M., Deeg, H. J., Alonso, R., Bouchy, F., & Rouan, D. 2008, A&A, 491, 889
Djupvik, A. A., & Andersen, J. 2010, in Highlights of Spanish Astrophysics V, ed. J. M. Diego, L. J. Goicoechea, J. I. González-Serrano, & J. Gorgas (Berlin: Springer), 211
Dobbs-Dixon, I., Lin, D. N. C., & Mardling, R. A. 2004, ApJ, 610, 464
Droege, T. F., Richmond, M. W., & Sallman, M. 2006, PASP, 118, 1666
Fabrycky, D., & Tremaine, S. 2007, ApJ, 669, 1298
Ford, E. 2006, ApJ, 642, 505
Ford, E. B., & Rasio, F. A. 2008, ApJ, 686, 621
Fortney, J. J., Baraffe, I., & Militzer, B. 2010, in Exoplanets, ed. S. Seager (Tucson, AZ: Univ. Arizona Press), 397
Fortney, J. J., Lodders, K., Marley, M. S., & Freedman, R. S. 2008, ApJ, 678, 1419
Fortney, J. J., Marley, M. S., & Barnes, J. W. 2007, ApJ, 659, 1661
Gandolfi, D., et al. 2010, A&A, 524, A55
Hansen, B. M. S., & Barman, T. 2007, ApJ, 671, 861
Hartman, J. D., Bakos, G. Á., Torres, G., et al. 2009, ApJ, 706, 785
Johnson, J. A., Winn, J. N., Cabrera, N. E., & Carter, J. A. 2009, ApJ, 692, L100
Kipping, D. M. 2010, MNRAS, 407, 301
Kipping, D. M., & Bakos, G. Á. 2011, ApJ, 730, 50
Koch, D. G., Borucki, W. J., Rowe, J. F., et al. 2010, ApJ, 713, L131
Kovács, G., Bakos, G. Á., Hartman, J. D., et al. 2010, ApJ, 724, 866
Kovács, G., Bakos, G. Á., & Noyes, R. W. 2005, MNRAS, 356, 557
Kovács, G., Zucker, S., & Mazeh, T. 2002, A&A, 391, 369
Latham, D. W. 1992, in ASP Conf. Ser. 32, IAU Colloq. 135, Complementary Approaches to Double and Multiple Star Research, ed. H. A. McAlister & W. I. Hartkopf (San Francisco, CA: ASP), 110
Leconte, J., Baraffe, I., Chabrier, G., Barman, T., & Levrard, B. 2009, A&A, 506, 385
Levrard, B., Winisdoerffer, C., & Chabrier, G. 2009, ApJ, 692, L9
Mandel, K., & Agol, E. 2002, ApJ, 580, L171
Marcy, G. W., & Butler, R. P. 1992, PASP, 104, 270
Maxted, P. F. L., Anderson, D. R., Collier Cameron, A., et al. 2010, PASP, 122, 1465
McCullough, P. R., Stys, J. E., Valenti, J. A., et al. 2005, PASP, 117, 783
Moutou, C., Diaz, R. F., Udry, S., et al. 2011, A&A, 533, A113
Naef, D., Latham, D. W., Mayor, M., et al. 2001, A&A, 375, L27
Pál, A. 2009a, MNRAS, 396, 1737
Pál, A. 2009b, PhD thesis, Eötvös Loránd Univ.
Pál, A., & Bakos, G. Á. 2006, PASP, 118, 1474
Pál, A., Bakos, G. Á., Torres, G., et al. 2008, ApJ, 680, 1450
Perryman, M. A. C., Lindegren, L., Kovalevsky, J., et al. 1997, A&A, 323, L49
Pollacco, D. L., Skillen, I., Collier Cameron, A., et al. 2006, PASP, 118, 1407
Pourteau, A. 1933, Catalogue des étoiles doubles de la zone +24 degrés de la Carte Photographique du Ciel, Observatoire de Paris (Orleans: H. Tessier)
Queloz, D., Anderson, D., Collier Cameron, A., et al. 2010, A&A, 517, L1
Queloz, D., Bouchy, F., Moutou, C., et al. 2009, A&A, 506, 303

Schlaufman, K. C. 2010, ApJ, 719, 602
Schneider, J., Dedieu, C., Le Sidaner, P., Savalle, R., & Zolotukhin, I. 2011, A&A, 532, A79
Shkolnik, E., Aigrain, S., Cranmer, S., et al. 2009, in AIP Conf. Proc. 1094, Cool Stars, Stellar Systems, and the Sun, ed. E. Stempels (Melville, NY: AIP), 275
Skiff, B. A. 2009, VizieR Online Data Catalog, 1, 2023
Skrutskie, M. F., Cutri, R. M., Stiening, R., et al. 2006, AJ, 131, 1163
Southworth, J., Hinse, T. C., Dominik, M., et al. 2009, ApJ, 707, 167
Sozzetti, A., Torres, G., Charbonneau, D., et al. 2007, ApJ, 664, 1190
Sozzetti, A., Torres, G., Charbonneau, D., et al. 2009, ApJ, 691, 1145
Spiegel, D. S., Burrows, A., & Milsom, J. A. 2011, ApJ, 727, 57
Tingley, B., & Sackett, P. D. 2005, ApJ, 627, 1011
Torres, G., Bakos, G. Á., Hartman, J., et al. 2010, ApJ, 715, 458
Torres, G., Bakos, G. Á., Kovács, G., et al. 2007, ApJ, 666, L121
Torres, G., Neuhäuser, R., & Guenther, E. W. 2002, AJ, 123, 1701
Udry, S., Mayor, M., Naef, D., et al. 2002, A&A, 390, 267
Valenti, J. A., & Fischer, D. A. 2005, ApJS, 159, 141
Valenti, J. A., & Piskunov, N. 1996, A&AS, 118, 595
Vaughan, A. H., Preston, G. W., & Wilson, O. C. 1978, PASP, 90, 267
Vogt, S. S., Allen, S. L., Bigelow, B. C., et al. 1994, Proc. SPIE, 2198, 362
Winn, J. N., Fabrycky, D., Albrecht, S., & Johnson, J. A. 2010, ApJ, 718, L145
Yi, S., Demarque, P., Kim, Y.-C., et al. 2001, ApJS, 136, 417